Crack Development in Cross-Ply Laminates Under Uniaxial Tension

Andrew L. Gyekenyesi
Cleveland State University
Cleveland, Ohio

January 1996

National Aeronautics and
Space Administration

Trade names or manufacturers' names are used in this report for identification only. This usage does not constitute an official endorsement, either expressed or implied, by the National Aeronautics and Space Administration.

CRACK DEVELOPMENT IN CROSS-PLY LAMINATES UNDER UNIAXIAL TENSION

Andrew L. Gyekenyesi
Cleveland State University
Cleveland, Ohio

SUMMARY

This study addresses matrix-dominated failures in carbon fiber/polymer matrix composite laminates in a cross-ply lay-up. The events of interest are intralaminar fracture in the form of transverse cracks in the 90° plies and longitudinal splitting in the 0° plies and intralaminar fracture in the form of 0/90 delamination. These events were observed using various nondestructive evaluation (NDE) techniques during static tensile tests. Acoustic emission (AE), x radiography, and edge view microscopy were the principal ones utilized in a real-time environment. A comparison of the NDE results with an analytical model based on the classical linear fracture mechanics concept of strain energy release rate as a criterion for crack growth was performed. The virtual crack closure theory was incorporated with a finite element model to generate strain energy release rate curves for the analytical case. Celion carbon fiber/polyimide matrix (G30-500/PMR-15) was the material tested with cross-ply lay-ups of $(0_2/90_6)_s$ and $(0_4/90_4)_s$.

The test specimens contained thermally induced cracks caused by the high-temperature processing. The analytical model was updated to compensate for the initial damage and to study further accumulation by taking into account the crack interactions. By correlating the experimental and analytical data, the critical energy release rates were found for the observable events of interest.

CHAPTER I

INTRODUCTION

Composite materials have become established as workable engineering materials and are now quite commonplace around the world. Because of their high stiffness-to-weight ratios, fiber-reinforced, laminated composite materials are increasingly replacing conventional materials in a wide array of structures. Multilayered filamentary composites exhibit great potential as structural materials in space vehicles, deep submergence vessels, radomes, and other applications where they excel. With their outstanding mechanical properties combined with their unique flexibility in design and ease of fabrication, it is no wonder that their use has surpassed that of other materials.

Laminated composite systems are constructed by stacking several plies, or layers. For a carbon/polymer continuous fiber system, the plies consist of high-strength carbon fibers embedded in a low-strength, low-density polymer matrix material while the matrix is in its molten state. Subsequently, the system is cured at specified pressures and temperatures, resulting in a very light yet sturdy material. The underlying structural principle for these materials is that the fibers be the primary load-carrying members while the matrix provides the structural integrity by serving as a load-transferring medium, providing rigidity and protecting the fibers from exposure to unfavorable environments.

The strength of a composite depends on the orientation of the fibers with respect to the direction of the maximum anticipated stress. Alignment of the filaments with the direction of the maximum stress utilizes the material most efficiently. The ability to carry a load is greatly reduced as the angle of the applied stress deviates from the direction of the fibers (longitudinal) and reaches a minimum capability at 90° (transverse). It is not uncommon for a ply to have a breaking stress and stiffness in the transverse direction one-fiftieth of that in the longitudinal direction. Likewise, the longitudinal coefficient of thermal expansion is much smaller than the transverse.

Because the applied loads are not always unidirectional, laminate lay-ups are constructed so that the plies are aligned in multiple directions. The difference in arrangement of the individual plies in a laminate causes internal stresses and strains due to a Poisson's effect during loading. Also, the thermal expansion mismatch results in differential contraction between the laminae on cooling to ambient temperatures subsequent to elevated temperature curing or postcuring operations.

In the case of $(0/90)_s$ cross-ply types, matrix cracks in the 90° ply, known as transverse cracks, have been observed to occur at levels as low as 20 percent of the ultimate laminate tensile strain as shown by Harrison and Bader (1983) and by Flaggs and Kural (1982). Because the final rupture of the laminate is primarily controlled by the 0° plies whose ultimate tensile strain can exceed 1 percent, matrix cracking of this kind has often been tolerated in design as some benign internal failure mode.

Wang, Chou, and Lei (1984) stated that the formation of intraply matrix cracking signifies the beginning of a complex sublaminate crack development process. In the case of the cross-ply laminates, the onset of 90° ply transverse cracking is followed by multiple cracks in that ply if the tension is monotonically increased. These matrix cracks in the transverse ply can precipitate matrix cracks in other plies, as discussed by Bailey, Curtis, and Parvizi (1979). For instance, intraply splitting of the 0° ply can form parallel to the applied tension and cross over the 90° ply transverse cracks. Under an ascending load, 0° ply splitting can occur in multiple locations. The interaction of the two cracks gives rise to a highly magnified, three-dimensional stress field which develops at the intersection of the two crossing cracks. Bailey, Curtis, and Parvizi (1979) and Reifsnider et al. (1983) proposed that the interlaminar tensile and shearing components in this stress field can cause 0/90 interface delamination. At some critical load level, propagation of the many localized delaminations results in a massive 0/90 interface separation which is often the last matrix cracking event before catastrophic failure. Wang, Kishore, and Li (1985) stated that laminates of more practical lay-ups suffer a similar matrix crack development process although the sequence of events may be different. Bailey, Curtis, and Parvizi (1979) discussed experiments which have generally established that the entire process is a generic phenomenon unique to the laminate type and the nature of the load. Although such a statement implies the possibility for some form of analytical description, success has been achieved only for laminates of simpler forms.

Wang and Crossman (1980) described the basic mechanisms of 90° ply transverse cracking under monotonic tension by an application of the energy release rate concept of classical fracture mechanics. Multiple cracks in the 90° ply were explained by Wang, Chou, and Lei (1984), who used a stochastic procedure incorporating the concept of effective flaw distribution as an inherent ply material property. Free-edge delamination was also modeled by Wang, Slomiana, and Bucinell (1983) using this approach.

2

The next step taken by Wang, Kishore, and Li (1985) was to analytically model matrix cracks in multiple plies and their mutual interactions. This modeling was accomplished by using a finite element routine to analyze the stress fields near several important crack interaction regions and then employing the same routine to simulate any possible crack growth resulting from the interactions. Using experimental data from Crossman, Warren, and Wang (1983), Wang et al. demonstrated that the load-dependent processes of matrix cracking and crack interaction at high loads could be analytically described by a three-dimensional stress analysis and by a crack growth simulation based on the techniques of fracture mechanics.

Wang, Kishore, and Li (1985) verified the above technique using an undamaged graphite-epoxy system. In the study, they successfully predicted the onset of transverse cracks, longitudinal splitting, and 0/90 delaminations; the latter initiated from the crossing of the transverse and splitting cracks.

In the present investigation, the system of crack interaction was more complex in the specimens because of pretest damage due to residual stresses incurred during high-temperature processing. The data from the experimental and analytical portions of the study were correlated to obtain the critical energy release rate values for the events of interest. A carbon fiber/polyimide matrix (G30-500/PMR-15) composite system was employed. The observable pretest damage consisted of 90° transverse cracks, 0° splitting, and small-angled cracks in the 90° plies located at the base of the transverse cracks.

The experimental portion of this investigation implemented nondestructive evaluation (NDE) methods to study the events of interest and the sequences of damage leading to final failure. Acoustic emission (AE), x radiography, and edge view microscopy were the three techniques utilized for the real-time observations of the cracking events. The material and testing equipment are discussed further in chapter II.

For the analytical portion, the three-dimensional finite element model was updated to more closely represent the physical system and its initial cracks. Strain energy release rate curves were produced to study crack growth and crack interactions in the cross-plies. The modified numerical model consisted of a significantly finer mesh than that employed in the studies mentioned earlier. Chapter III introduces Wang's theory and the finite element procedure employed for the carbon/polyimide system. A general description of classical fracture mechanics is also presented.

The results of the experimental and analytical portions of the study are given in chapter IV with a comparison and full discussion. Also, the feasibility of the acoustic emission method to distinguish between the matrix-dominated events is discussed as is the effectiveness of the other techniques.

Chapter V summarizes this effort and indicates future directions. Experimental observations revealing unexpected events are mentioned with respect to future considerations. Recommendations for improvements in both the experimental and analytical methods are also presented.

3

CHAPTER II

EXPERIMENTAL METHOD

In this study, static tensile tests were conducted on carbon fiber/polyimide matrix (G30-500/PMR-15) laminates. The specimens were tested to obtain the basic laminae properties. Then followed a thorough investigation of their behavior in cross-ply lay-ups of the form $(0_2/90_6)_s$ and $(0_4/90_4)_s$. The ply properties were employed in the analytical solution of the system. Transverse cracks in the 90° plies, splitting in the 0° plies, and delaminations between the 0° and 90° plies were the events of interest examined in the cross-plies. Acoustic emission, x radiography, and edge view microscopy were the real-time NDE techniques used to observe the specimens. By employing these methods, the specimens did not have to be removed from the load frame during inspection, which in turn eliminated any possible fatigue damage that would have occurred during reloading.

The carbon/polyimide system employed for this study had extensive damage prior to tensile testing. A considerable amount of splitting, transverse cracks, and shear-induced angled cracks at the base of the transverse cracks were noted for both specimen types. This damage was caused by the residual stresses induced by the high curing temperature during fabrication. Papadopoulos and Bowles (1990) and Simpson, Jacobs, and Jones (1991) present a more thorough analysis and explanation of the thermal strains inherent in this material when it is laminated in a cross-ply lay-up. In chapter IV, typical examples of the initial pretest damage are presented.

The objective of the experiments was to study the accumulation of further damage to the composite system during monotonic loading and to study the behavior of the cross-plies prior to ultimate failure. By employing the NDE techniques mentioned earlier, the occurrence of subsequent events was recorded in real time, thus giving an accurate portrait of further crack propagation.

Materials

The polyimide laminates were made with Ferro CPI-2237 prepreg (G30-500/PMR-15) and fabricated into the laminates of interest by the Polymer Branch of the Materials Division at the NASA Lewis Research Center. Prepregnated tapes were made by drum winding (12 turns/in.) and impregnating graphite fibers with a PMR-15 solution. Table I summarizes the properties of the G30-500 carbon fibers (BASF Structural Materials Incorporation) and polyimide matrix material (NASA Lewis Research Center) as stated by their respective manufacturers. The dimensions of the panels were 7.62 by 25.4 cm with a fiber volume fraction of 0.60. Each prepregnated stack was then placed in a preforming mold and staged for 1 hr at 204 °C. After staging, the stack was placed in a matched metal die. The composite was then molded by placing the die in a press heated to 316 °C and applying a pressure of 3.45 MPa when the die temperature reached 232 °C. After the temperature reached 316 °C, the pressure and the temperature were maintained for 2 hr. The laminate was then cooled and removed from the mold when the temperature regressed to 232 °C.

The panels were cut into test size specimens (dimensions summarized in table II and fig. 2.1), and last, tapered glass epoxy end tabs were attached. The average single ply thickness was 1.41×10^{-2} cm.

TABLE I.—BASIC PROPERTIES OF FIBER AND
MATRIX MATERIALS

Properties	G30–500 fibers	PMR–15 matrix
Tensile strength, MPa	3620	90
Tensile modulus, GPa	234	3.5
Ultimate elongation, percent	1.4	2.0
Poisson's ratio		
Longitudinal	0.20	0.35
Transverse	.25	.35
Density, g/cm^3	1.77	1.22
Equivalent yarn cross-sectional area, cm^2	2.3×10^{-3}	– – –

TABLE II.—DIMENSIONS OF SPECIMENS

Lay-up	Length, cm			Thickness, cm		Gage, area, cm^2
	Specimen, L	Gage, L$_G$	Width W, cm	Specimen, t,	End tab T	
$(0_2/90_6)_s$	25.3	17.7	2.18	0.216	0.43	0.471
$(0_4/90_4)_s$	25.3	17.7	2.18	.213	.43	.465
(0_8)	25.3	17.7	2.24	.112	.33	.245
(90_8)	14.0	6.40	2.24	.107	.36	.239
$(\pm45)_{2s}$	25.3	17.7	2.24	.112	.33	.245
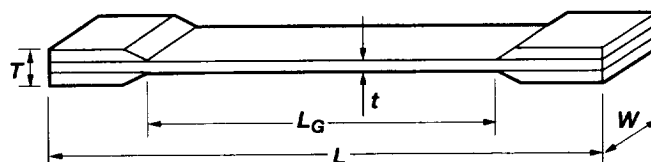
Figure 2.1.—Specimen geometry.

Procedure

All the specimens had longitudinal and transverse electrical resistance strain gauges attached to provide load-versus-strain plots. M-Bond 200 adhesive was employed to attach the gauges at a central location aligned longitudinally and transversely on the face of the specimen. Trial runs with gauges applied to both faces of the specimen confirmed that there was no bending in the specimen; hence, only two gauges on a selected face were required. Finally, one edge of each sample was polished for edge view microscopy observation using 200-grit sandpaper followed by 400 and 600 grits.

The tension testing was performed on a screw-driven Instron 8500 dynamic load frame with an upper limit of 50 000 N. The tests were completed under load control with rates varying from 445 to 1335 N/min. The entire study was conducted at a room temperature of 21±3 °C and an ambient relative humidity of 60±5 percent. The setup is shown in figures 2.2 and 2.3.

Lamina Tensile and Shear Response

Determination of the basic ply properties was the first step in the experimental portion of this study. They were obtained by performing static tensile tests on three elementary lay-ups as explained by Carlsson and Pipes (1987). For the longitudinal properties, a (0_8) laminate was employed, for transverse properties, a (90_8), and for shear characteristics, a $(\pm45)_{2s}$. In each case, at least three specimens were tested and their results averaged.

The measured material properties included

E_1 Young's modulus in the fiber direction

E_2 Young's modulus transverse to fiber direction

G_{12} in-plane shear modulus

$\gamma_{12,ult}$ ultimate in-plane shear strain

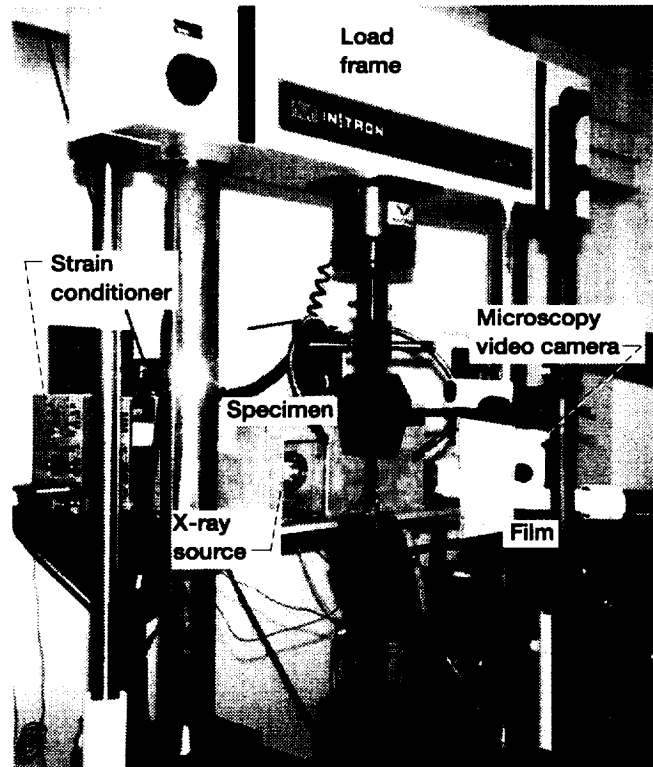$\varepsilon_{1,ult}$ ultimate tensile strain in fiber direction
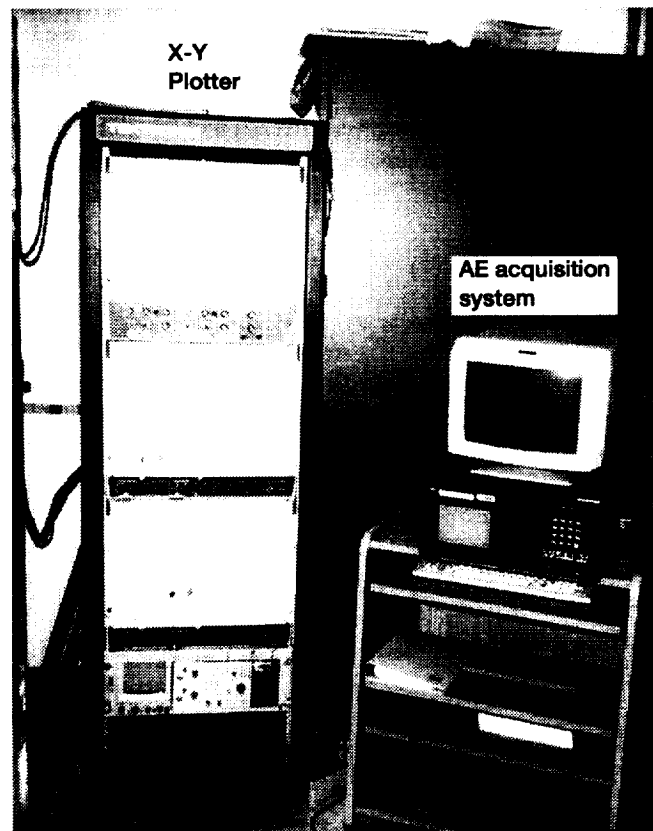
Figure 2.2.—General view of test facilities.

Figure 2.3.—Data collection devices used during testing.

$\varepsilon_{2,ult}$ ultimate tensile strain transverse to fibers

v_{12}, v_{21} Poisson's ratios

$\sigma_{1,ult}$ ultimate tensile stress in fiber direction

$\sigma_{2,ult}$ ultimate tensile stress transverse to fibers

τ_{ult} ultimate in-plane shear stress

Damage Inspection of Cross-Plies Using NDE

Determination of the load and strain at the addition or propagation of longitudinal splitting, transverse cracking, and 0/90 delaminations in the cross-plies of the form $(0_2/90_6)_s$ and $(0_4/90_4)_s$ was the primary objective of the testing. In all cases at least three tests were completed and the results averaged. The damage mechanisms of interest were detected by using three NDE techniques: acoustic emission, fluorescent-dye-enhanced x radiography, and optical microscopy with real-time video taping of the edge view.

Acoustic emission.—Acoustic emission data were collected during the mechanical testing. The equipment implemented was manufactured by Physical Acoustic Corporation (PAC). Two transducers (Micro-30, with a nominal resonance frequency of 250 kHz) were attached using a viscous couplant and electrical tape. A 40-dB preamplifier (1220 A) with a plug-in filter of 100 kHz to 1.2 MHz was used with the two sensors. The output from the preamplifier was fed to a signal acquisition system (Locan AT, fig. 2.3) that had the threshold set at 45 dB. The hit definition time for signal recognition was 1000 μs.
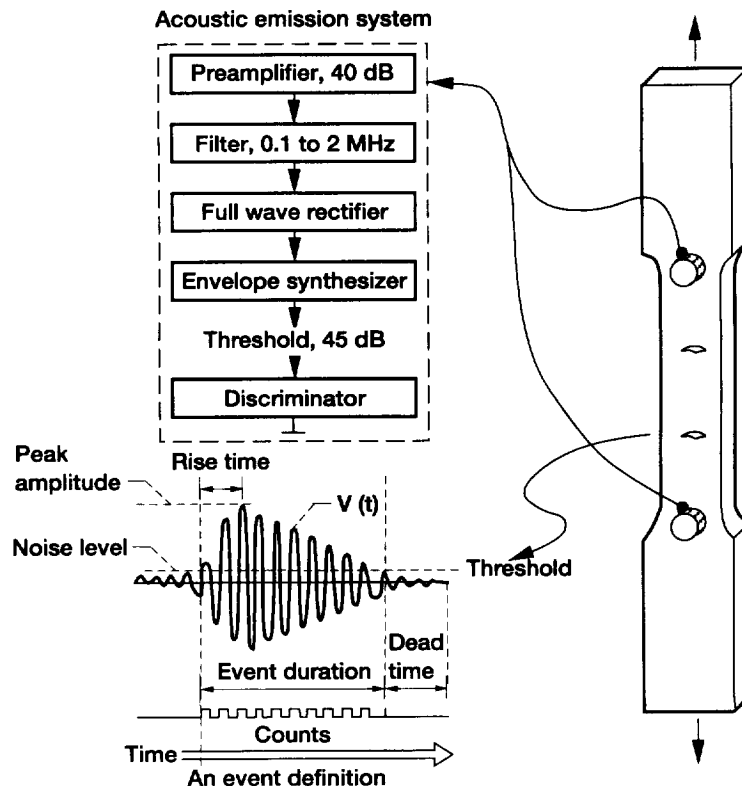

Figure 2.4.—Terminology for an acoustic event.

The terminology of an acoustic event is given in figure 2.4. The AE parameters utilized in this study were peak amplitude and energy. The energy of an AE signal is measured in relative units and is expressed as

$$E = \frac{1}{R} \int_0^\infty [V(t)]^2 dt \qquad (2.1)$$

where R is the resistance input impedance of the voltage measuring circuit and $V(t)$ is the time-dependent voltage. Because E is a time integral, it can capture attenuation effects to some extent. Further, the energy measured is the energy of the electrical signal generated by the transducer. It is neither the energy in the acoustic wave nor the mechanical energy (energy release rate) released by the actual failure events.

For identifying the events of interest, an attempt was made to distinguish event signals by correlating them to the other NDE data. Results of an AE study on kevlar/epoxy cross-plies by Rajan, Kishore, and Agarwal (1989) demonstrated peak amplitude as the best indicator for characterizing the damage mechanisms. In another study by Jeng, Kanji, and Yang (1989), it was shown that the AE signals generated by a carbon/polyimide system closely resembled those recorded for carbon/epoxy and thermoplastic composites.

Duesing (1989) and Rajan, Kishore, and Agarwal (1989) proposed that a distinct range of amplitude peaks was produced by the different failure events. For resin cracking, most events tended to be in the low amplitude range whereas delaminations had separate peaks which occurred midrange in the distribution. Finally, fiber breakage was conspicuous in the data because it emitted high amplitude events and exhibited a distinct peak on the amplitude distribution plot. Also, the energy of the event helped to distinguish transverse cracks from splitting due to the longer duration and higher energy of the 0° ply event.

In a study by Awerbuch, Perkinson, and Kamel (1980), a thorough investigation of a carbon/polyimide composite was conducted. In the investigation, several NDE methods were employed to examine the behavior of the composites in various lay-ups. The AE method was among the techniques utilized. From the results of the tensile tests, Awerbuch and others were able to differentiate fiber breaks from matrix failures by using the amplitude level of the event signal. Even so, the conclusion of the study was that no correlation could be made between the specific matrix failure event and the amplitude distribution characteristics for the carbon/polyimide system.

X Radiography.—The in situ x-ray technique was used to record information periodically and was used to monitor all the damage events of interest. Because the unique setup had the x-ray source located on the test rig, the specimen did not have to be removed for an exposure. In taking the x rays, a Phillips 160-kV constant potential source was used with a setting of 35 kV and 10 mA. The x-ray source/generator was capable of a maximum voltage of 160 kV and a maximum current of 45 mA. "On the fly" exposure time was 35 sec. The source was located 22.9 cm from the composite specimen and 30.5 cm from the film giving a 1.2 magnification (see figs. 2.2 and 2.3). To enhance the detection of defects, a sodium iodide dye penetrant was applied to the specimens. The exposures were taken every 2225 N or when AE showed a high intensity of event occurrences. A schematic of the setup is given in figure 2.5.

Edge view microscopy.—The principal NDE technique utilized in this study was edge view microscopy. This technique was used to obtain the majority of the information on transverse cracks and edge delaminations. Simple sight observations with a magnifying glass were used to follow the 0° splitting of the cross-plies because the edge view did not carry this information.

Rather than gather data periodically as is usually the case with edge view microscopy, real-time observations were made. A charged coupled device (CCD) Sony high-resolution video camera was used with an Olympus stereo microscope (Model SZ60 with a maximum magnification of 60) to view the specimen edge (fig. 2.6).

The microscope and the video camera were focused on a fixed area of the polished specimen edge. Information was recorded and stored using a video recorder (VCR). A correlation between the video recording and the load was made by relating the load rate to the time counter of the VCR. The area of focus on the specimen edge was approximately 0.254 by 0.254 cm. It was assumed that this area was a good representation of the entire specimen when numerous specimens (three or four for each laminate) were averaged.
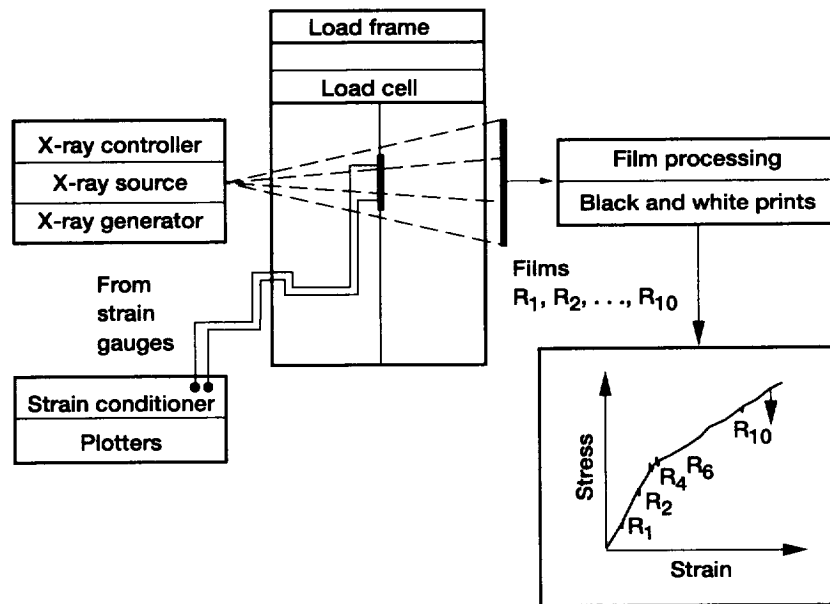
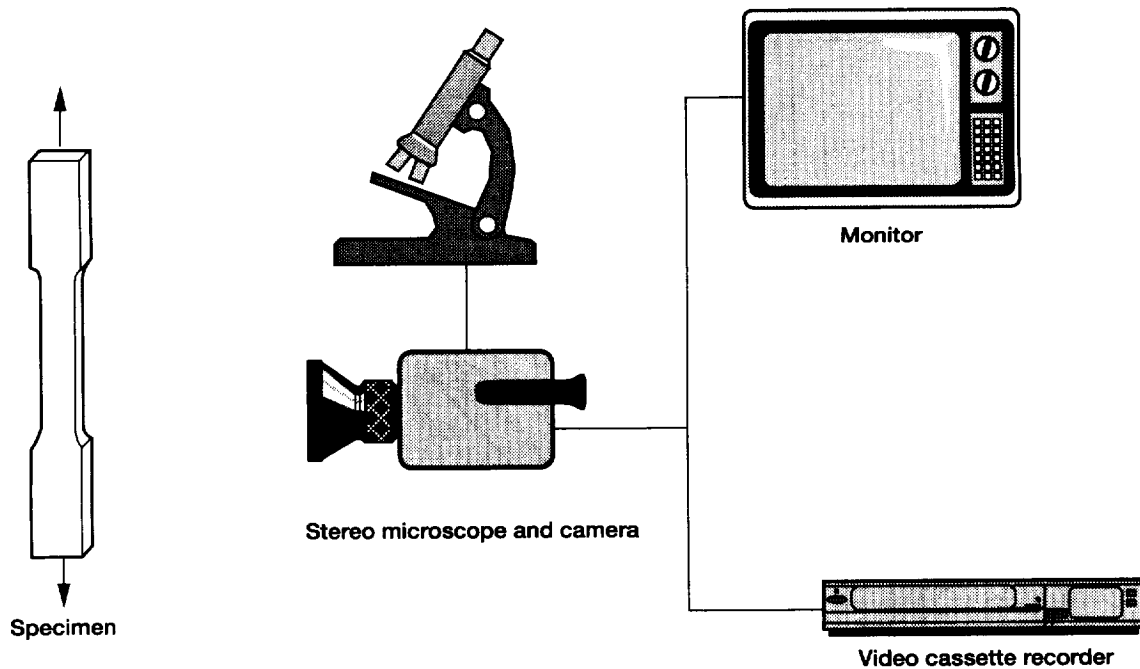Figure 2.5.—In situ x-ray and materials testing system (Baaklini (1992)).

Figure 2.6.—Real-time edge view microscopy apparatus.

9

CHAPTER III

THEORETICAL BACKGROUND

The types of damage that are most frequently observed in fibrous composite laminates are the results of matrix-dominated cracks. The first of these is transverse cracking which occurs in plies whose fibers are oriented transverse to the applied load. The second type is longitudinal splitting in which the crack forms parallel to the fiber direction when a displacement restriction in the transverse direction of the plies is imposed by the lay-up of the other plies. The third type, interply delamination, is usually found near the free edge of the laminate or at the intersections of transverse and longitudinal cracks. These events are schematically presented in figure 3.1. The cracks and their growth are detrimental to the structural reliability and the durability of the laminate and may lead to ultimate failure. In this chapter, the cracks of interest are discussed and described with respect to the strain energy release rate technique of classical fracture mechanics.

Multiple transverse cracks form in plies when a sufficiently large tensile stress exists transverse to the fibers. For example, Wang and Crossman (1980) considered the cross-ply (0/90) laminate. When under a uniaxial tension in the 0° direction, the 90° plies may suffer multiple cracks that usually occur at a relatively low strain level. Wang and Crossman stated that existing design practices generally employ a two-dimensional laminate analysis and calculate the stresses and strains in the individual laminae. The onset of cracks is inferred from the calculated stresses or strains. They went on to say that this approach has not provided a fully satisfactory description of the transverse cracking process.

In a study by Bader et al. (1979), cross-ply (0/90) graphite epoxy laminates having different 0/90 thickness ratios were tested under uniaxial tension. They found that transverse cracks occurred at different strain levels depending on the thickness of the 90° plies. They also showed that the tensile strain at the onset of multiple cracking increased consistently with decreasing 90° ply thickness. In Bader's investigation, an energy consideration advanced earlier by Aveston and Kelly (1973) was used to relate the onset of transverse cracking and the available energy release for a fully developed crack. The procedure employed by Aveston and Kelly successfully described the trend between the 90° ply thickness and the onset of transverse cracking. This ply thickness dependence was believed to stem from the ply interactions in the laminate.

Delamination between plies is another mode of matrix-dominated failure that involves ply structural interactions in the laminate, as discussed by Wang and Crossman (1980). The existence of interlaminar stresses, usually
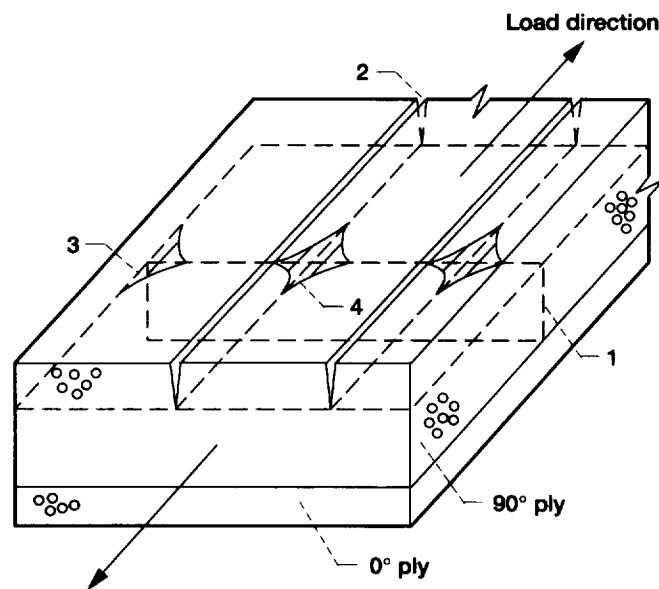
Figure 3.1.—Matrix-dominated cracking events. (1) Transverse crack. (2) Longitudinal splitting. (3) Free-edge 0/90 delamination. (4) 0/90 Delamination induced by crossing cracks.

10

found near the free edges of the laminate, are assumed to cause delaminations. Wang, Kishore, and Li (1985) conducted a finite element analysis to determine the out-of-plane stress σ_z acting on the 0/90 interface for cross-plies of the form $(0_2/90_2)_s$ and $(0_2/90_4)_s$. He found that this stress was tensile at the free edge and along any existing transverse crack roots. He also noticed that the magnitude of σ_z depended on the thickness or volume of the 90° plies.

In the case of transverse cracks, Wang declared that the dependence on thickness could not be explained by a simple stress analysis. This approach would predict the same strain value for the onset of cracking independent of the 90° ply thickness. He found that the observed thickness effect on the threshold strain for ply delamination and transverse cracking may be explained from an energy point of view. He reasoned that the actual amount of strain energy in the plies of a laminate and the manner of its release during a damage event play an important role in the crack initiation and the crack growth behavior.

The strain energy release rate concept of classical fracture mechanics was employed by Rybicki, Schmueser, and Fox (1977) to describe the behavior of free-edge ply delamination. Wang, Chou, and Lei (1984) based their use of the concept on the assumption that small cracks or interlaminar defects exist in the laminate. These flaws propagate when the required condition is met for the crack to extend. Rybicki showed that the growth of the defects existing near the ply interface/free-edge region is stable initially; that is, the applied load must be increased to extend the delamination. The quantity measuring the material resistance to a crack event is the critical energy release rate G_C for the particular event. When stable crack growth occurs and a new crack surface is created, the release of strain energy is experienced. The rate of available energy per unit crack surface G can be calculated by an elastic stress analysis. The available strain energy G is viewed as the driving force for further crack extension which occurs when $G = G_C$. If $G < G_C$, the crack remains stationary until the applied load is increased, whereas the crack growth becomes unstable when $G > G_C$.

Computationally, there are numerous ways to evaluate the energy release rate. Wang and Crossman (1980) explained that G is generally a complicated function of crack location, crack geometry, ply stacking sequence, ply properties, ply thickness, and applied loads. Because of the analytical complexity, the most practical approach for calculating G was presented by Rybicki and Kanninen (1977). They used a finite element analysis in conjunction with a crack closure technique. The event of interest in their study was free-edge delamination at the 0/90 interface in cross-ply laminates. The main assumptions of the analytical and numerical models were that edge delamination involved only matrix-dominated fracture, which was assumed elastic and brittle, and that the crack path was parallel to the ply interface. The numerical procedure involved introducing a virtual crack of known dimension and computing the work needed to close it.

The energy release rate concept and the finite element analysis employed by Rybicki were further developed by Wang, Kishore, and Li (1985) to also include 90° transverse cracks, 0° splitting, and 0/90 interface delaminations. A finite element model was constructed to calculate the energy release rates of each event individually or to simulate further crack development due to their interactions. In each case, a theory was formulated on the basis of conceptual and physical considerations. For this investigation, further refinements were made to the finite element model. These revisions of the three-dimensional FE model were made to better replicate the pretest-damaged high-temperature carbon fiber/polyimide matrix system of interest.

Description of Energy Release Concept

In classical fracture mechanics (see Broek, 1986), it is assumed that energy is dissipated when a new crack surface is created within a stressed body. Crack growth arises at manmade or naturally occurring flaws. The strain energy dissipation normalized with respect to crack surface depends on the material and is denoted as the critical energy release rate G_C. Furthermore, G_C is a function of the crack mode. In general, three types of crack modes exist: the opening (mode I) and the shearing (modes II and III). These events can occur simultaneously as mixed modes (I-II, I-III, etc.). The three crack mode events (I, II, and III) are illustrated in figure 3.2.

For a crack to extend, there must be enough strain energy in the material to induce further growth. As pointed out earlier, the available strain energy is denoted by G and is viewed as the driving force for further crack extension. One method of calculating G is to determine the energy dissipated when a crack extends an infinitesimal amount. The energy release rate is defined for this type of virtual crack extension as

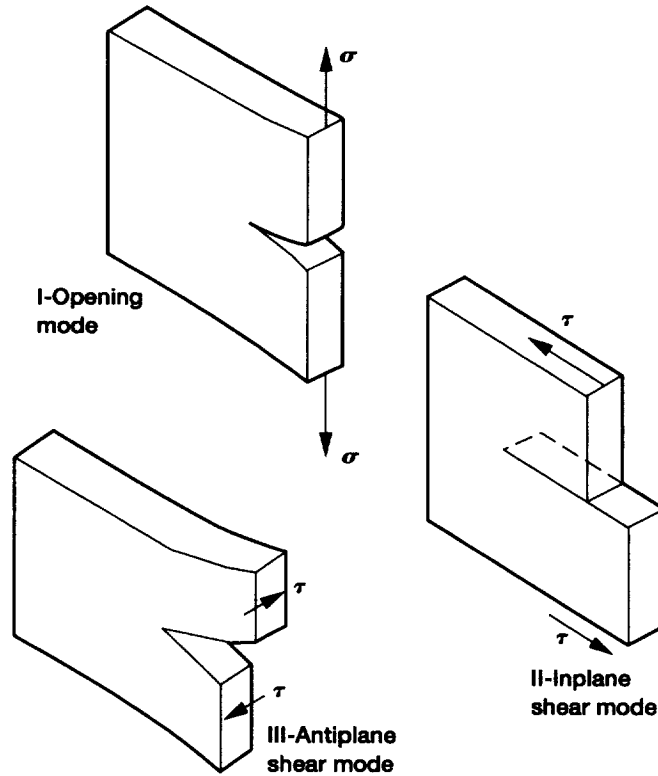$$G = \frac{dW}{da} - \frac{dU}{da} \qquad (3.1)$$

Figure 3.2.—Standardized crack extension modes.

where W accounts for the work of any externally applied tractions per unit width, U is the accumulated strain energy of the body per unit width, and a is the initial crack length. The physical significance of the energy release rate corresponds to the rate of change of the system energy per unit area of crack growth. Accordingly, the development of the fracture model for sublaminate cracks rests on the ability to accurately calculate G and physically measure G_C for a given failure mode.

When taken as a criterion for crack growth, the energy release rate also provides a means of identifying stable crack growth, as discussed by Rybicki, Schmueser, and Fox (1977). Stable crack growth can be considered in terms of the shape of the curve which shows energy release rate versus crack length. Rybicki explained that a monotonically increasing curve (fig. 3.3) indicates unstable crack growth. Consider a flaw with an initial crack length a_o. The critical value of G associated with crack extension corresponds to the load P_o. As the crack extends to $a_o + \Delta a$, the curve indicates that the amount of energy available to drive the crack exceeds the critical value G_C. Thus, the crack will continue to grow in an unstable fashion. Rybicki also gave an illustration of a stable crack growth in figure 3.4. Again, the critical value of P for crack extension is denoted by P_o. However, as the crack grows to a length $a_o + \Delta a$, the amount of available energy to drive the crack decreases to a value below the critical value of G_C. The crack continues to grow to length a_{cr}. At this point, the crack will not propagate until the load is increased above P_o. With a crack length of a_{cr}, an increase in load to the critical level will induce an unstable growth because of the upward trend of the curve.

Rybicki stated that there are numerous ways to evaluate the energy release rate. With the exception of several simple component geometries with simple boundary conditions, the direct evaluation of G from equation (3.1) can be quite complex. A more practical computational procedure uses the definition of G in terms of the crack closure integral as described by Rybicki and Kanninen (1977).
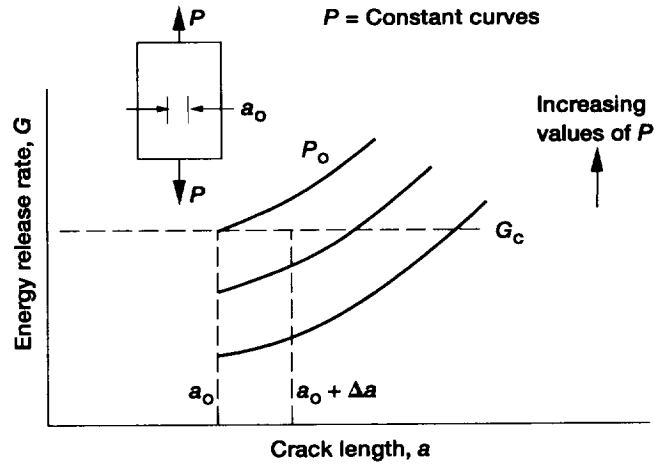
12

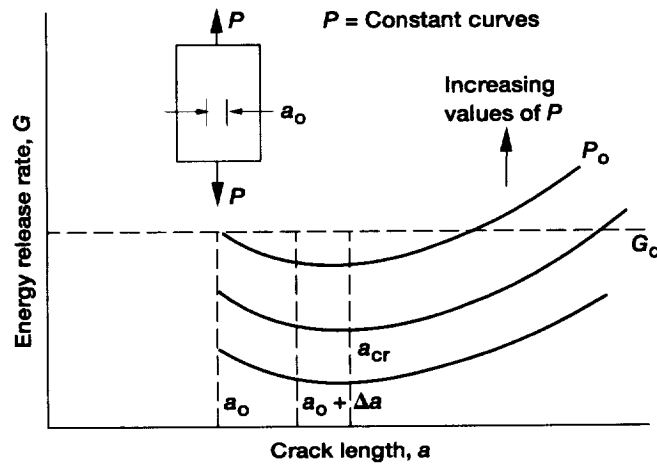Figure 3.3.—Energy release rate versus crack length for unstable crack growth (Rybicki, Schmueser, and Fox (1977)).

Figure 3.4.—Energy release rate versus crack length for stable crack growth (Rybicki, Schmueser, and Fox (1977)).

Calculation of Available Energy Release Rate

Analytical solutions for the available energy release rate are difficult to obtain because the stress field found at the tip of the crack has a singularity. This singularity requires tedious mathematical derivations. Direct solution methods for G are available; among them are the well-known J-integral and the virtual crack closure proposed by Irwin (1958).

Irwin observed that the strain energy released during a virtual extension of an existing flaw is equal to the work required to close it. The closing of the virtual crack extension Δa yields the solution for the required surface traction vector Σ distributed over Δa. The work done can be expressed as

$$G = \lim_{\Delta a \to 0} \frac{1}{2\Delta a} \int_0^{\Delta a} (\Sigma \cdot \Delta u)\,\mathrm{d}a \qquad (3.2)$$

13

where Δu is the relative crack surface displacement vector acting along the incremental length Δa. Note that both Σ and Δu depend on the crack size a and the applied far-field stress.

If the crack extension involves all three modes (I, II, and III), the vector product of equation (3.2) will give a sum of three scalars associated respectively with G_I, G_{II}, and G_{III}. Irwin's method also has the distinct advantage of being particularly adaptive to finite element techniques. Specifically, Rybicki and Kanninen (1977) employed a finite element model to evaluate G for a line crack in a plane. The crack tip stress traction Σ and the displacement vector Δu in equation (3.2) are approximated by the nodal forces and displacements, respectively.

Consider a laminate having a finite width and a stacking sequence such that tensile interlaminar normal stress σ_z is induced near the free edge when a far-field tensile strain e_o is applied. Next, assume that an effective interlaminar flaw of size a exists along the edge as illustrated in figure 3.5. When the free-edge stress reaches a critical value, the crack will propagate. As explained by Wang, Slomiana, and Bucinell (1983), this event constitutes the onset of free-edge delamination, and the concurrent stress state is termed the threshold stress.

Figure 3.5 depicts a typical G-curve for an assumed flaw size a obtained by the finite element crack closure procedure. For a given value of e_o, G is dependent on the flaw size as shown in the figure. It is seen that G rises sharply from zero at $a = 0$, and reaches an asymptotic value G_m at $a \geq a_m$. The value of a_m is usually of the order of the ply thickness. If a laminate is subjected to a far-field strain of e_o, and a sublaminate crack is simulated, the crack-tip energy release rate can be expressed in the general form

$$G_e = C_e \cdot t \cdot e_o^2 \tag{3.3}$$

where t is the linear scale between the actual physical model and the finite element model. The value for t is usually taken as one ply thickness. The coefficient function C_e, which is a function of the nondimensional crack length a/t, is calculated by imposing a far-field strain of $e_o = 1$ on the finite element model.

A thermal strain due to a temperature change ΔT can also induce a crack extension. The equation relating ΔT and the energy release rate can be expressed as

$$G_T = C_T \cdot t \cdot (\Delta T)^2 \tag{3.4}$$

where C_T is also a function of a/t. The entire C_T curve is generated numerically by imposing $\Delta T = -0.56\ °C\ (-1\ °F)$.

Combining equations (3.3) and (3.4) gives the total energy release rate due to an applied far-field strain and the temperature load. The combined effects are represented as
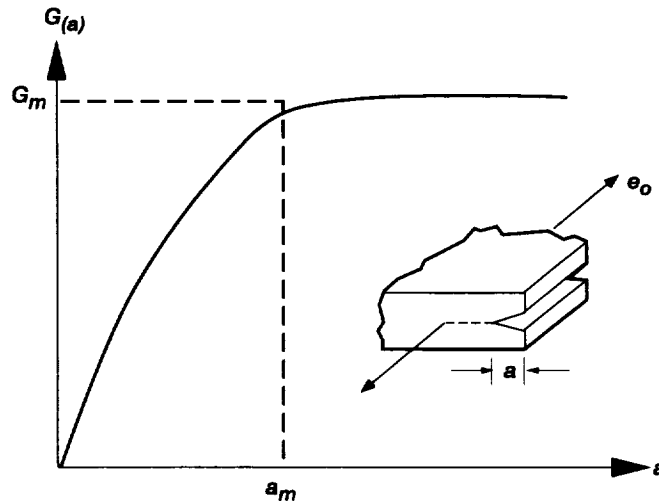

Figure 3.5.—Typical shape of energy release rate G(a) for edge delamination (Wang and Crossman (1982)).

14

$$G = \left[(C_e)^{\frac{1}{2}} \cdot e_o + (C_T)^{\frac{1}{2}} \cdot \Delta T \right]^2 t \qquad (3.5)$$

Both coefficient functions C_e and C_T are independent of the applied load. Thus, the functions are characteristic for a particular type of crack growth and are denoted as the energy release rate coefficient functions.

In practice, polyimide-based laminates are subjected to extensive thermal residual strains after curing. The effects of the residual stresses can be evaluated by assuming a uniform temperature change

$$\Delta T = T - T_o \qquad (3.6)$$

Equation (3.6) represents the difference between the processing stress-free temperature and the working temperature.

Virtual Crack Closure Technique

Rybicki and Kanninen (1977) used the crack closure integral to evaluate G_I and G_{II} employing the virtual crack closure technique (VCCT). They evaluated the mode I and mode II crack closure integrals from equation (3.2) utilizing nodal forces and displacements from two successive finite element runs. Figure 3.6 illustrates a simple two-dimensional finite element representation of a crack-tip region. Here, a crack of length a is shown with the crack tip at node c. The finite element solution determines the displacement components $(u,v,w)_c$ of the crack tip node c. An incremental crack extension Δa is introduced by replacing the crack-tip node c with two separate nodes f and g as shown in figure 3.6. With this new crack geometry taken into account, the finite element solution for nodal displacements $(u,v,w)_f$ and $(u,v,w)_g$ is found for nodes f and g, respectively. The crack extension is then closed by applying equal and opposite forces at nodes f and g such that their common displacements match the displacement found earlier for node c. These forces are actually the internal nodal forces which existed at node c before it was opened.

The work required to close the crack extension is approximated by

$$\Delta W \approx \frac{\left[F_x \left(u_f - u_g \right) + F_y \left(v_f - v_g \right) + F_z \left(w_f - w_g \right) \right]}{2} \qquad (3.7)$$

where F_x, F_y, and F_z are the components of the nodal forces required to close the nodes f and g together. Thus, the energy release rates for the three crack extension modes are approximated by
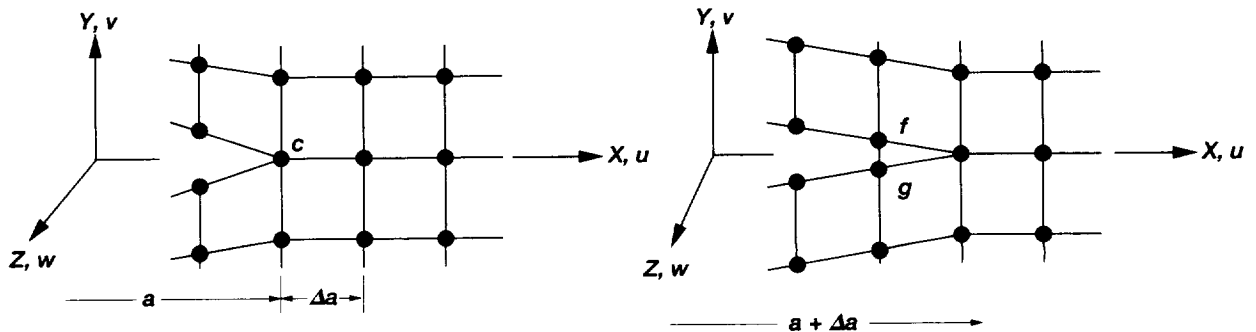

Figure 3.6.—Finite element mesh at crack tip illustrating crack closure technique (Wang and Crossman (1982)).

15

$$G_I \approx \frac{F_y\left(v_f - v_g\right)}{2\Delta a}$$

$$G_{II} \approx \frac{F_x\left(u_f - u_g\right)}{2\Delta a}$$

$$G_{III} \approx \frac{F_z\left(w_f - w_g\right)}{2\Delta a}$$

(3.8)

The main advantage of the VCCT is that it requires only the use of simple continuum elements. This eliminates much of the difficulty with inverse square root singularity elements which were previously utilized at the crack tip when solving fracture mechanics problems by the finite element method (Broek, 1986).

For this study, experimental results were correlated with analytical data to calculate the critical strain energy release G_C for the events of interest. The value of G_C was found by implementing equation (3.5). The threshold strain of a specific cracking event was obtained from tensile tests and was combined with the coefficient strain release rate functions produced by the finite element analysis to calculate G_C for a particular damage sequence.

The values of G_C are dependent on the specific cracking event, the crack propagation path, the laminate lay-up, and the method of loading for the specimen. As shown in Wang and Crossman (1982), the total critical energy release rate is also a function of the crack mode ratios $(G_{IC}/G_{IIC}, G_{IC}/G_{IIIC},$ etc.; see eq. (3.8)). Although G_C varies for the different matrix-dominated cracks, the values are of the same magnitude. Hence, comparisons of the C_e and C_T curves for the different events can give information about their sequence of occurrence.

Finite Element Model

The numerical procedure (see Wang, Kishore, and Li (1985)) employed for the present analysis utilizes a computer code which was developed for independent and self-contained operation. The main function of the program is to numerically simulate the initiation and growth of a plane crack in a three-dimensional solid, specifically, transverse cracking, delamination, splitting, or delamination with a split in composite plates. The plate may be subjected to mechanical loading, thermal loading, or both.

During crack extension, the changes in the boundary conditions as the crack grows are automatically adjusted in the program. There is no limitation to the number of layers or the stacking sequence. The layers may have different thicknesses and material properties. Each layer is assumed to be a homogeneous, orthotropic elastic medium with one of its principal axes aligned in the thickness direction of the plate (z-axis).

The algorithm contains three independent programs: the preprocessor, the main code, and the postprocessor. The preprocessor requires input data regarding the specimen geometry, the finite element mesh plan, the layer material properties, the boundary conditions, and the double nodes (double nodes are a pair of nodal points which occupy the same spatial position). The output of the preprocessor contains information pertaining to the finite element mesh (i.e., the numbered nodes and the double nodes). The output is then supplemented with the crack-opening-sequence data set.

The main code (KSAP II) performs the numerical calculations in the solution of the three-dimensional finite element model using an 8- or 21-node solid element with three degrees of freedom (x,y,z) for each node. The output data from the preprocessor and the crack-opening-sequence data serves as the input for this program and crack extension is simulated in a step-by-step fashion. At each increment, the program computes the released energy as well as the stress and displacement fields.

The KSAP II code has the capability to simulate crack opening along the surface which passes through the points where double nodes are prescribed. Initially, the nodes are assigned equal displacements and the system of linear equations is solved with the appropriate boundary conditions. The nodal forces, the nodal displacements and the stresses at the prescribed locations in each element are also calculated. The nodal forces of the double nodes are the internal forces holding those two nodes together. The crack opening is simulated by releasing the boundary

16

conditions of the double nodes (their displacements are no longer equal). Once again, the system of linear equations is solved. The difference in the displacements between the two nodes will be the crack-opening displacement. The internal forces which held the nodes together (found in the preceding iteration) can be used to compute the strain energy release as the crack opening is simulated through the node. This procedure is continued until all the double nodes are opened. Hence, the strain energy released as the crack passes through successive double nodes can be calculated at each step. At each step, the crack opening can be simulated through one or more pairs of double nodes, and there is no limitation on the crack front shape. If the crack is simulated along a symmetric plane (i.e., transverse cracks), there is no need for double nodes in that plane. The crack extension can be simulated by simply changing the boundary conditions of the nodes on that plane from zero displacement to free-force boundary conditions.

Finally, the energy release rates are calculated by dividing the energy released during the crack growth by the area of the crack extension at a particular iteration. The values of C_e and C_T can be derived by simply dividing the energy release rates by the normalizing factor, which in this case is the thickness of one ply t. The output data from KSAP II contains the details of the finite element mesh as well as the solution of the laminated plate for the given crack simulation.

For the model in this study, 3220 elements were utilized. The solid 21-node elements had three degrees of freedom (x, y, z) for each node. A value of one was employed for the scale factor t of equation (3.5). Because of symmetry, only one-quarter of the plate cross section was modeled (see fig. 3.7). An initial transverse crack was represented for each case by having zero load boundary conditions on one end of the model for the 90° plies. The sequence for nodal release was chosen to produce the maximum energy release and was determined by numerous trial and error runs.

Figures 3.8 and 3.9 depict the nodal release sequences which produced the maximum strain energy release for the split-induced and free-edge-induced delaminations. The secondary transverse crack was located at a centered location in the finite element model; it was initiated at the midplane and propagated towards the 0° plies. The 0° split was initiated at the end containing the initial transverse crack and was propagated parallel to the induced load.
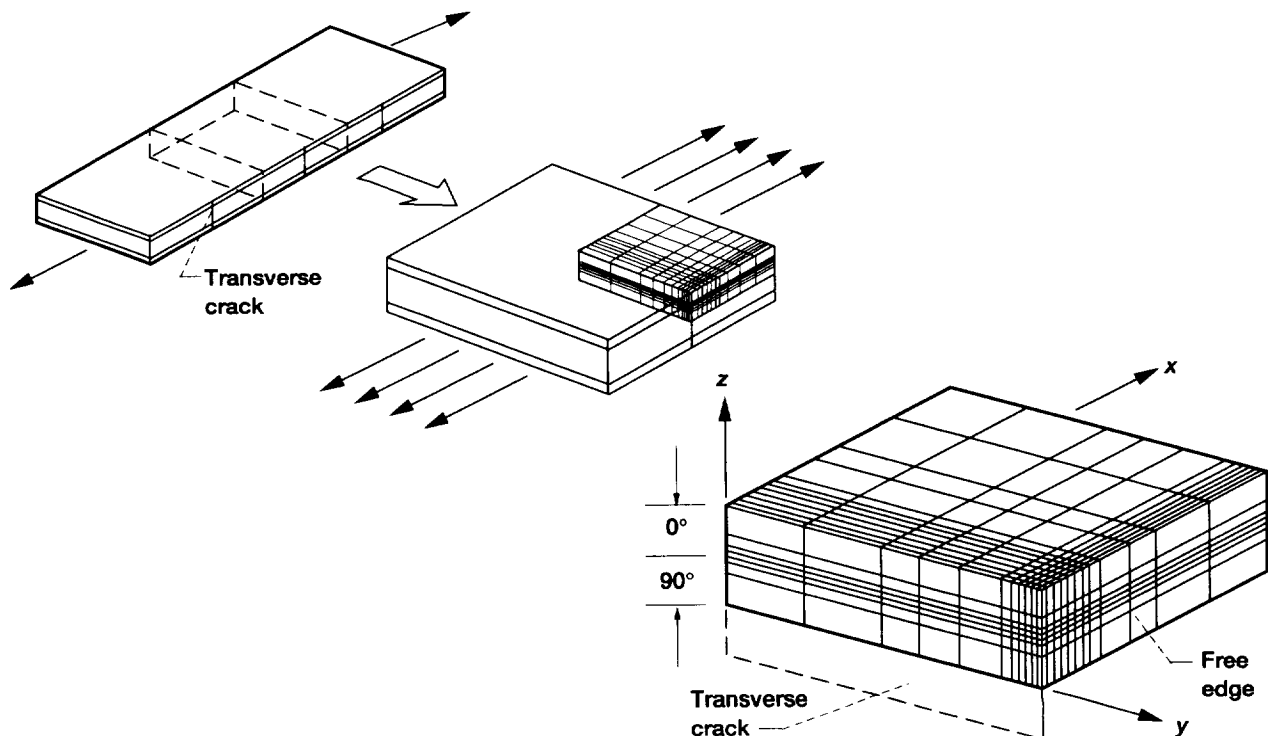

Figure 3.7.—Finite element network for symmetric laminate modeled with initial transverse crack (Wang, Kishore, and Li (1985)).
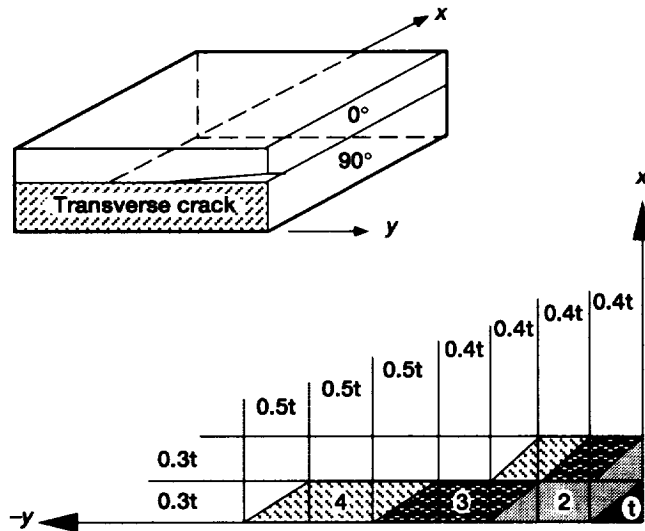
Figure 3.8.—Contoured delamination near free-edge/transverse crack corner point and nodal release sequence for delamination simulation.
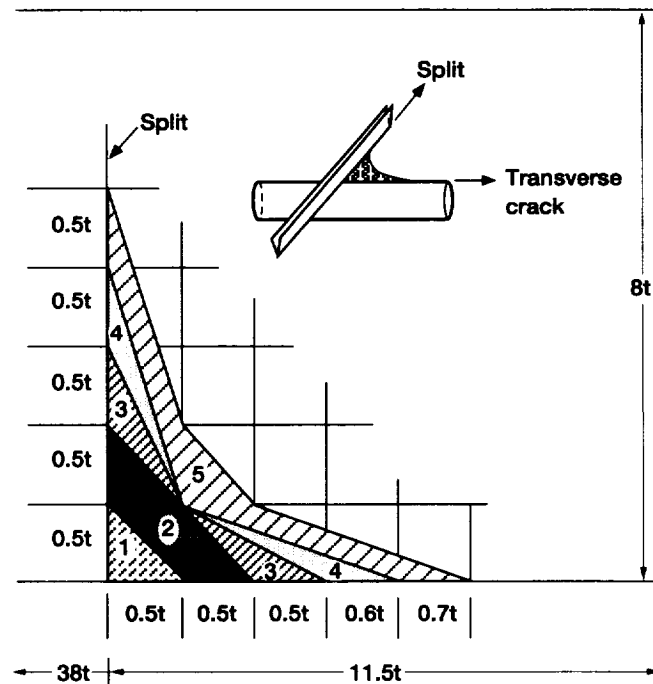

Figure 3.9.—Contoured delamination at cross crack and nodal release sequence for delamination simulation.

18

CHAPTER IV

DISCUSSION OF RESULTS

In this chapter, a description of the results obtained from the experimental and analytical portions of the study is presented. The basic ply properties are given, and the observed behavior of the cross-plies is discussed. By combining the experimental data with finite-element-produced strain energy release rate curves, the critical energy release rates were calculated for specific matrix-dominated events.

Experimental Results

For all the results reported in this chapter, each represents the averaged values from three or four replicate specimens. The data scatter for the experimental results is discussed in the text and the average values are displayed in the tables. The statistical nature of the data scatter is not discussed.

Basic Ply Properties

Tables III and IV present the basic ply properties, and figures 4.1 to 4.3 display the typical stress-versus-strain behavior of the laminates tested with the replicated averages given in the figure legend. The predicted values in table IV were calculated by using basic laminate equations found in any introductory composites course (see Agarwal and Broutman (1990)). For consistency, the subscript 1 was employed to represent the longitudinal direction for the experimental results; the subscript 2, for the in-plane direction; and the subscript 3, for the out-of-plane direction.

The rule of mixtures was utilized for predicting values of E_1, $\sigma_{1,ult}$, $\varepsilon_{1,ult}$, $\tau_{12,ult}$, $\gamma_{12,ult}$, and v_{12}. The Halpin-Tsai equations were employed for calculating E_{12} and G_{12}. For determining $\sigma_{2,ult}$ and $\varepsilon_{2,ult}$, the strength-of-materials approaches of stress concentration factor and strain magnification factor were used. Finally, v_{21} was found by the relationships between the engineering constants and the compliance matrix.

TABLE III.—FIBER VOLUME FRACTIONS

Lay-up	Fiber volume fraction (range)
$(O_2/90_6)_s$	0.60 (0.59 to 0.61)
$(O_4/90_4)_s$	.57 (.55 to .59)
(O_8)	.58 (.55 to .61)
(90_8)	.59 (.58 to .59)
$(\pm45)_{2s}$	.56 (.54 to .58)

TABLE IV.—MATERIAL CONSTANTS FOR CARBON FIBER/POLYIMIDE MATRIX (G30–500/PMR–15)

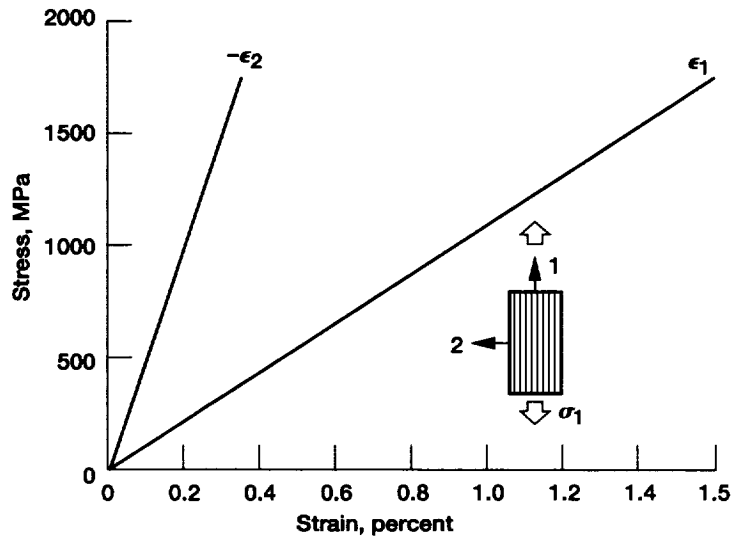| Properties	Experimental	Predicted
Modulus, GPa		
Tensile, E_1	123	139
Transverse, E_2	7.9	16
Shear, G_{12}	4.15	— — — —
Ultimate strength, MPa		
Tensile, $\sigma_{1,ult}$	1744	2137
Transverse, $\sigma_{2,ult}$	30.2	30.6
Shear, $\tau_{12,ult}$	58.5	— — — —
Poisson's ratio		
Major, v_{12}	0.25	0.26
Minor, v_{21}	.0077	.016
Ultimate strain, percent		
Tensile, $\varepsilon_{1,ult}$	1.5	1.5
Transverse, $\varepsilon_{2,ult}$	0.4	.34
Shear, $\gamma_{12,ult}$	2.2	— — — —

19

Figure 4.1.—Typical stress strain behavior for (0_8) longitudinal laminate (G30-500/PMR-15). Average of replicates: tensile modulus, E_1, 123 GPa; major Poisson's ratio, v_{12}, 0.25; ultimate tensile strength, $\sigma_{1,ult}$, 1744 MPa; ultimate tensile strain, $\epsilon_{1,ult}$, 1.5 percent.
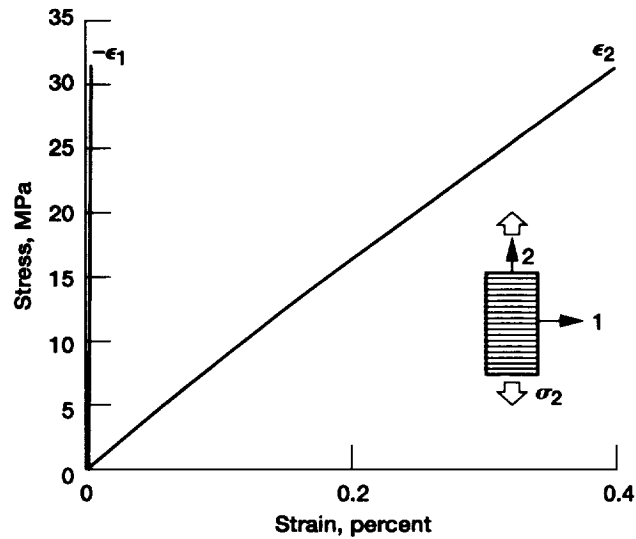

Figure 4.2.—Typical stress strain behavior for (90_8) transverse laminate (G30-500/PMR-15). Average of replicates: transverse modulus, E_2, 7.9 GPa; minor Poisson's ratio, v_{21}, 0.0077; ultimate transverse strength, $\sigma_{2,ult}$, 30.2 MPa; ultimate transverse strain, $\epsilon_{2,ult}$, 0.4 percent.
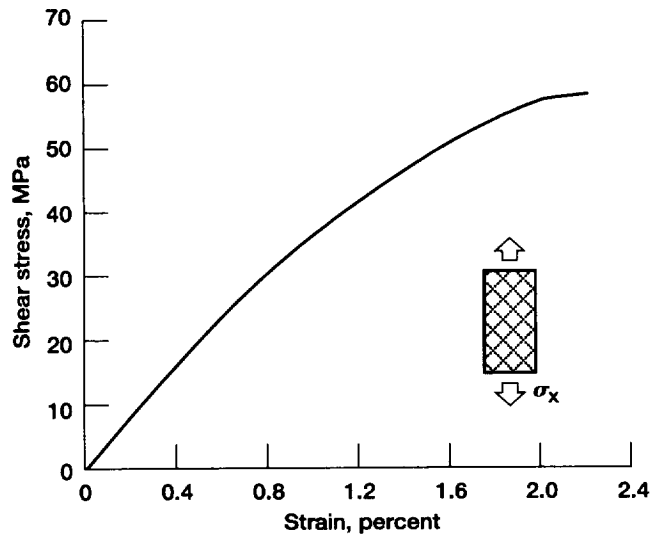
Figure 4.3.—Typical shear response obtained from $(\pm 45)_{2s}$ laminate (G30-500/PMR-15). Average of replicates: shear modulus, G_{12}, 4.15 GPa; ultimate shear strength, $\tau_{12,ult}$, 58.5 MPa; ultimate shear strain, $\gamma_{12,ult}$, 2.2 percent.

An observation of the experimental data for the (0_8) laminates revealed that the measured moduli varied by ± 5 percent from the experimental average for the group and exhibited linear behavior up to failure. The ultimate stress and ultimate strain had a scatter of ± 2 and ± 5 percent, respectively. As seen in table IV, the averaged results were lower than the predicted values.

For the unidirectional transverse plies (90_8), the individual moduli varied from the group average by ± 1 percent and exhibited linear behavior up to failure. A variation of ± 15 and ± 12 percent was recorded for the ultimate stress and strain, respectively. The experimental transverse modulus was 50 percent of the predicted value whereas the experimental ultimate strain was actually 17 percent higher. The strengths were within 1 percent.

The shear moduli, obtained using the $(\pm 45)_{2s}$ laminates, deviated by ± 5 percent from the average. The variance within the test group for the ultimate shear stress and the ultimate shear strain was ± 10 and ± 12 percent, respectively. Predicted values were not calculated because of the difficulty in obtaining the shear properties for the G30-500 carbon fibers.

The major Poisson's ratio of the specimens had a variation of ± 4 percent from the experimental average. The mean was 4 percent lower than the predicted value. The minor Poisson's ratio within the test group had a scatter of ± 7 percent from the average experimental value. This outcome for the minor ratio was one-half of the predicted result using the ratio $v_{12}/E_{12} = v_{21}/E_{21}$. The experimental data were used in the equation for the values of moduli and major Poisson's ratio. Inaccuracies of the transverse gauges at very small strains were the probable cause of the discrepancy. The transverse strains in the 90° unidirectional laminate only reached a maximum of 0.0031 percent.

A comparison of these ply properties with results of past studies that employed the same material system was conducted. The previous investigations were by Awerbuch, Perkinson, and Kamel (1980) and Papadopoulis and Bowles (1990). All the values were within a statistically acceptable range. Any variances were attributed to different fiber volume ratios and the quality of processing.

Finally, the coefficients of thermal expansion and the stress-free temperature were obtained from Papadopoulos and Bowles (1990). The average values for the longitudinal direction α_1 and transverse direction α_2 were -1.03×10^{-6} and $27.9 \times 10^{-6}/°C$, respectively; 346 °C was the average stress-free temperature.

Cross-Ply Damage Inspection Results

Among the three NDE methods chosen for the experimental portion of this study, only one was able to recognize the damage events of interest. The real-time edge view microscopy provided the most reliable source of

21

information. From this source, initial damage and any propagation from these cracks could be observed as the load was increased.

When the magnified edge view was examined, the propagation of a crack was either very obvious or was manifested in the bubbling of the fluorescent dye used to enhance the x-ray images. This dye leakage was usually the first sign of a localized 0/90 delamination growth at the base of a transverse crack. The photographs shown in this report are digitized images taken from the video tapes. Because of this transferring process, the quality of the picture was somewhat reduced; hence, the actual events shown may be difficult for the reader to interpret.

The in situ x-ray technique was excellent for studying the 90° ply transverse cracks and 0° ply splitting, although it was poor for interpreting the results of other events. The possible reason for this involved the width of the crack and the density of the sodium iodide dye penetrant. Because of the small size of some crack openings, the penetrant could not enter the crack space, making detection difficult.

The various matrix cracking events could not be discerned using the acoustic emission data. Amplitude, energy, and counts were plotted against strain and compared with observations of the edge view. No positive correlation could be made for the two techniques.

When working with materials with a high density of damage, the AE signals produced from further propagation of cracks can be altered by the gaps caused by the earlier damage. This attenuation effect can cause variations of the amplitude and energy signatures. However, distinct high-amplitude peaks were recorded in this study and were probably events of fiber breakage. A description of typical AE plots for each lay-up is presented later in this chapter.

Sequence of Cracking Events in Cross-Plies

As previously mentioned, as a result of high-temperature processing, both cross-ply lay-ups had extensive pretest damage in the form of 90° ply transverse cracks, 0° ply splitting, and shear-induced angled cracks at the bases of the transverse cracks. The purpose here was to study further accumulation of the damage and to determine the feasibility of using composite laminates which contain initial cracks.

Figures 4.4 and 4.5 show the pretest damage observed by using edge view microscopy. Seen in these figures are the transverse cracks surrounded by the shear-induced angled cracks. In both lay-ups, angled cracks existed at the bases of the transverse cracks. For the $(0_2/90_6)_s$ type, the angled cracks were observed at the bases of about half the transverse cracks, whereas the $(0_4/90_4)_s$ laminates had less frequent occurrences, at about one in four of the transverse cracks. These cracks were assumed to be induced by the interfacial shear stresses which exist in the vicinity of the transverse cracks in the 90° plies. Additional pretest high-magnification edge view observations (X200 and X400) were made to locate any other cracking events. No other damage events were noticed.

Presented in table V are the results for the cracking events observed in the cross-plies studied and figures 4.6 and 4.7 display typical stress-versus-strain plots for the two lay-ups. The averaged results of the replicates are given in the legend of each figure. Because both lay-ups exhibited linear behavior to failure, percent strain was used as the measurement to mark the time of the occurrence of an event. For each cross-ply lay-up, an initial test was loaded to failure. Also, one of the three fully observed replicates was stressed to failure. The data to calculate ultimate stresses and strains came from two specimens for each cross-ply type. The remaining replicates were loaded to a point where all the matrix damage sequences were experienced and further loading was unnecessary.

Saturation of 90° transverse cracks and 0° splitting was evident in both the $(0_2/90_6)_s$ and the $(0_4/90_4)_s$ lay-ups before tensile testing as shown by x rays of initial and near failure loads. These exposures presented in figures 4.8 and 4.9 show that no new transverse or longitudinal cracks occurred as the load was increased.

Figure 4.10 presents a schematic of the events which occurred as the cross-plies were loaded. For both lay-ups, the first cracking event to occur was the further accumulation of angled cracks. These cracks were assumed to initiate from unseen defects on the 0/90 boundary and propagated towards the major transverse crack. The height of these cracks was usually about one-third of the 90° layer thickness. The actual depth of the crack in the specimen could not be determined because the event could not be interpreted from the x radiographs. Figures 4.11 and 4.12 are the photographs of the angle cracks obtained from the real-time edge view microscopy. As expected, the $(0_2/90_6)_s$ laminate had a lower threshold strain level (0.46 versus 0.68 percent).
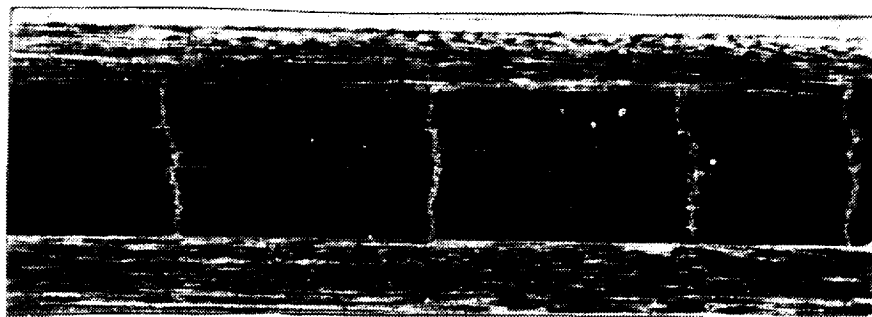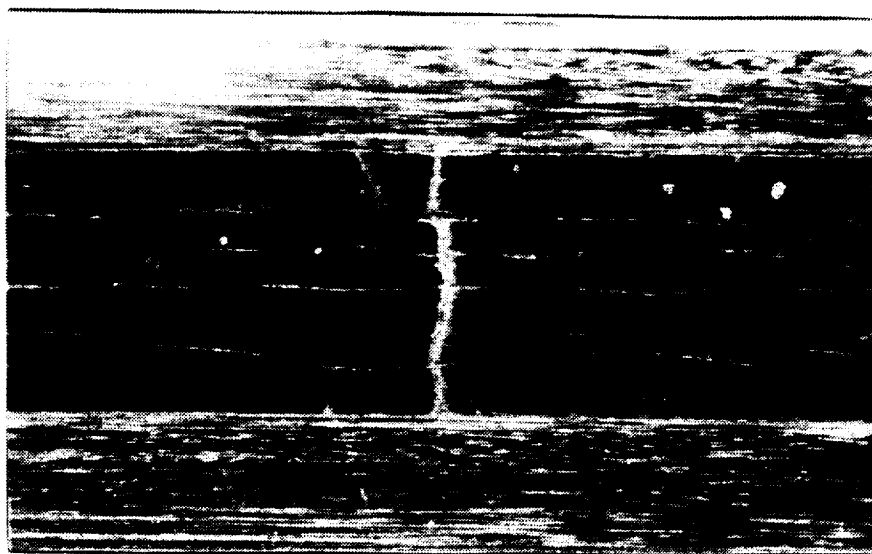
22
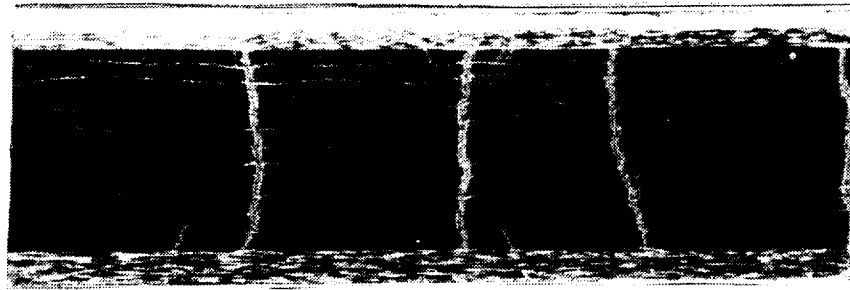
(a)
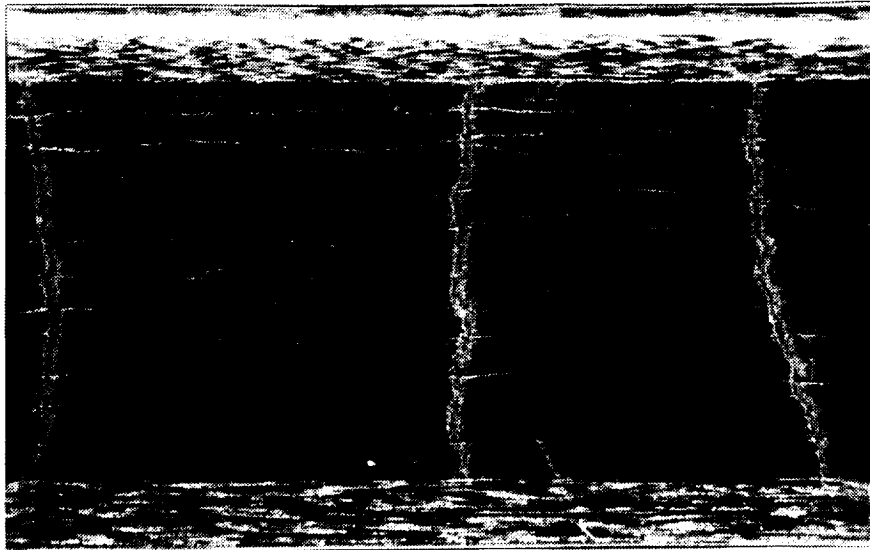
(b)

Figure 4.4.—Typical pretest edge view of $(0_2/90_6)_s$ laminate. (a) Magnification, 20.
(b) Magnification, 40.

(a)

(b)

Figure 4.5.—Typical pretest edge view of $(0_4/90_4)_s$ laminate. (a) Magnification, 20.
(b) Magnification, 40.

TABLE V.—SUMMARY OF CRACKING EVENTS

Lay-up	Experimentally observed event	Threshold strain, percent
$(0_2/90_6)_s$	Transverse cracking	(a)
	Longitudinal splitting	(b)
	Additional angled cracks	0.46
	0/90 Delamination	Onset at 0.69
	Localized fiber break	.74
	Ultimate failure	1.1
$(0_4/90_4)_s$	Transverse cracking	(c)
	Longitudinal splitting	(d)
	Additional angled cracks	0.68
	0/90 Delamination	Onset at 0.82
	Localized fiber break	1.0
	Ultimate failure	1.2

[a]Saturated before test, 12/in.
[b]Saturated before test, 15/in.
[c]Saturated before test, 16/in.
[d]Saturated before test, 10/in.

24
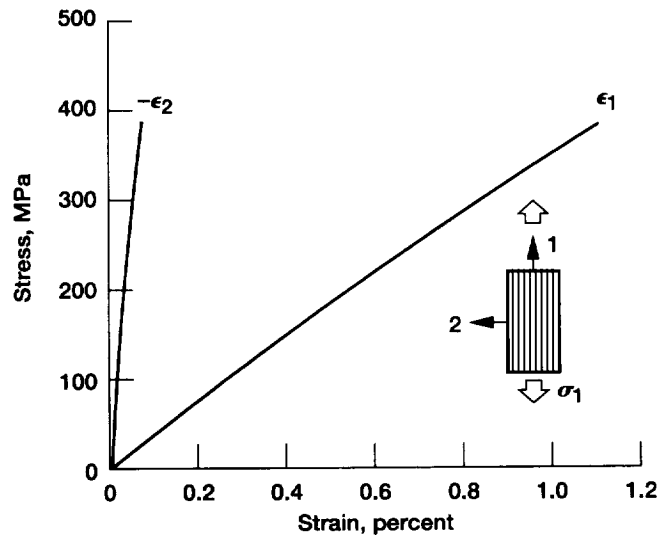
Figure 4.6.—Typical stress strain behavior for $(0_2/90_6)_s$ laminate (G30-500/PMR-15). Average of replicates: tensile modulus, E_1, 38.4 GPa; major Poisson's ratio, ν_{12}, 0.069; ultimate tensile strength, $\sigma_{1,ult}$, 383 MPa; ultimate tensile strain, $\epsilon_{1,ult}$, 1.1 percent.
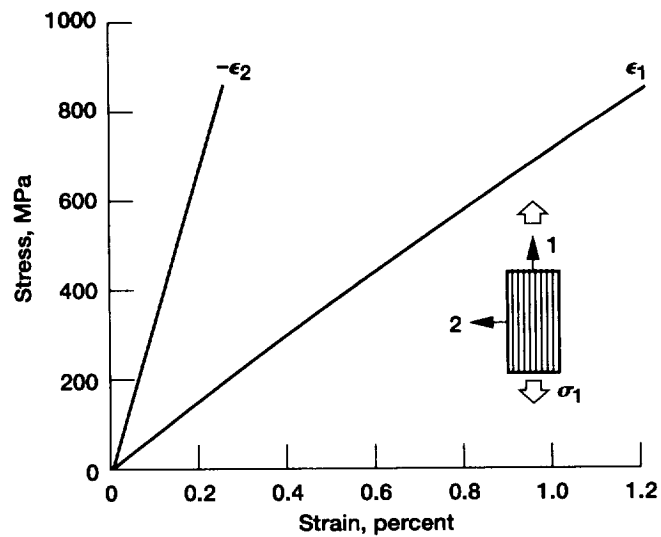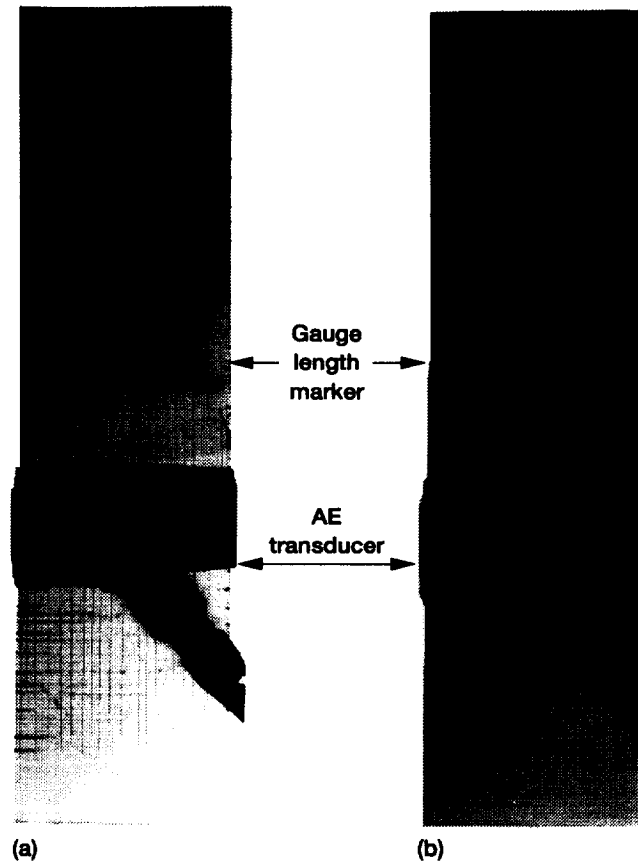

Figure 4.7.—Typical stress strain behavior for $(0_4/90_4)_s$ laminate (G30-500/PMR-15). Average of replicates: tensile modulus, E_1, 76.4 GPa; major Poisson's ratio, ν_{12}, 0.28; ultimate tensile strength, $\sigma_{1,ult}$, 840 MPa; ultimate tensile strain, $\epsilon_{1,ult}$, 1.2 percent.

25

Figure 4.8.—Radiographs of $(0_2/90_6)_s$ laminate displaying transverse and longitudinal cracks. (a) Initial pretest damage. (b) 0.90 percent strain.

Gauge
length
marker

AE
transducer

(a) (b)
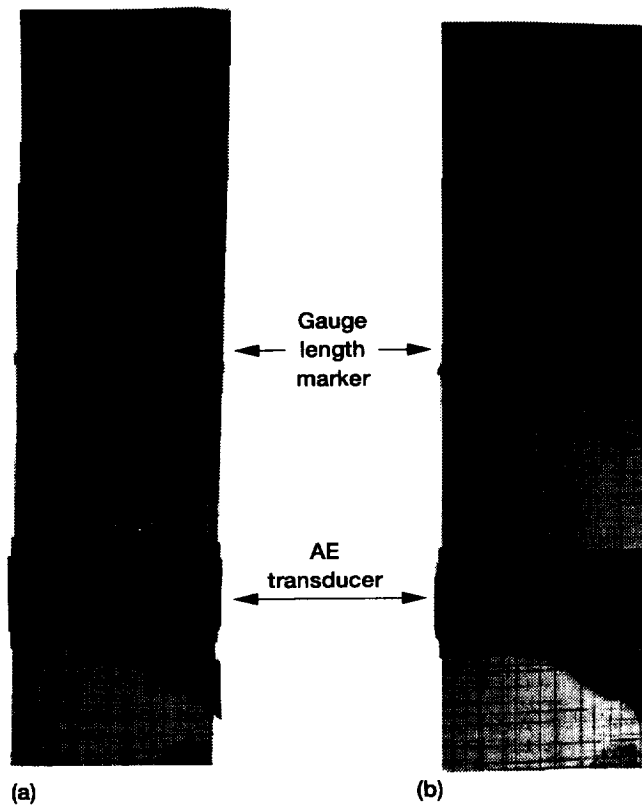
Figure 4.9.—Radiographs of $(0_4/90_4)_s$ laminate displaying
transverse and longitudinal cracks. (a) Initial pretest
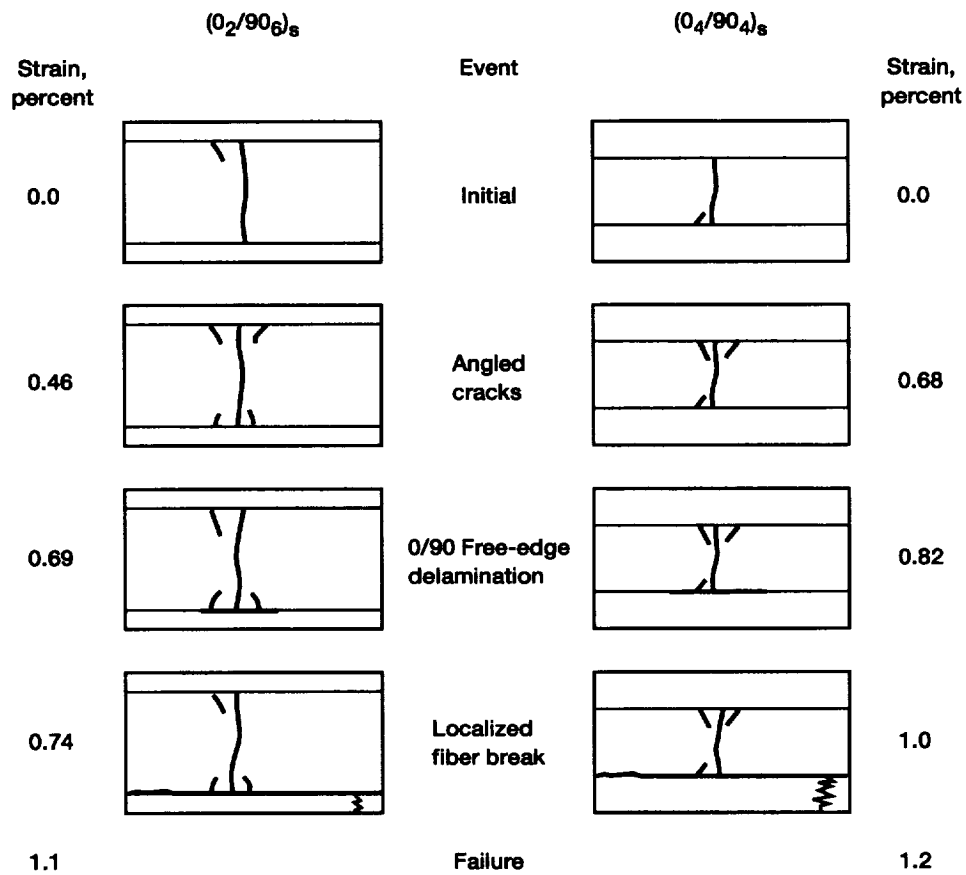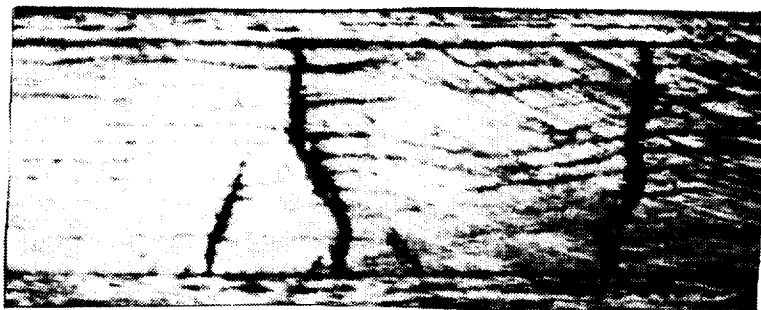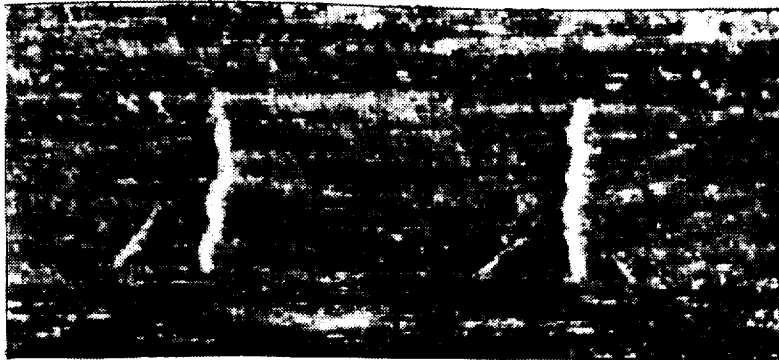damage. (b) 0.95 percent strain.

	$(0_2/90_6)_s$		$(0_4/90_4)_s$
Strain, percent		Event	Strain, percent
0.0		Initial	0.0
0.46		Angled cracks	0.68
0.69		0/90 Free-edge delamination	0.82
0.74		Localized fiber break	1.0
1.1		Failure	1.2

Figure 4.10.—Cracking sequence.

28

(a)

(b)

Figure 4.11.—Occurrence of angled crack in $(0_2/90_6)_s$ laminate. (a) Before.
(b) After.

(a)
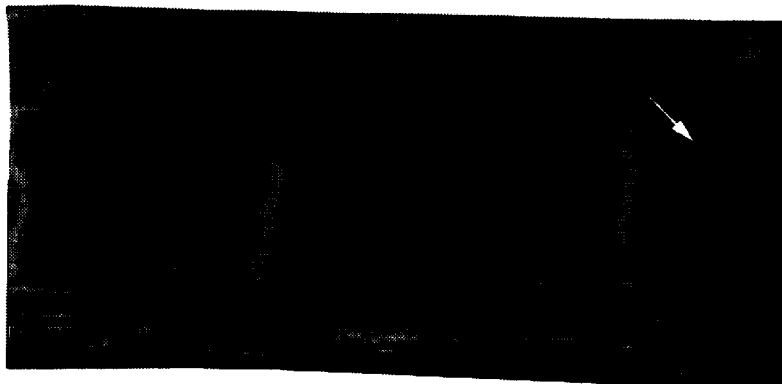
(b)

Figure 4.12.—Occurrence of angled crack in $(0_4/90_4)_s$ laminate. (a) Before. (b) After.

In the case of the $(0_2/90_6)_s$ plies, the mechanically induced angled cracks were recorded for two of the three specimens studied. The threshold strains for the two specimens were 0.40 and 0.51 percent. For the $(0_4/90_4)_s$ laminate, mechanically induced angled cracks were observed in all three of the replicas tested and ranged from 0.51 to 0.78 percent.

The next cracking event observed was the appearance of 0/90 edge delaminations. For both lay-ups, this event was first documented to occur at the bases of the transverse cracks which had no noticeable pretest localized delamination. Again, the depth of the delamination into the specimen could not be determined because the x rays could not detect the delaminations. Note that these events were difficult to observe, even when viewing the video tapes of the magnified edge view. The cracks appeared as a bubbling of the fluorescent dye; this dynamic action was lost in the transfer to photographs. Because the crack growth was unrecognizable in the static prints, no photographs of the localized delamination are presented. As expected, the event appeared at a lower strain in the $(0_2/90_6)_s$ than in the $(0_4/90_4)_s$ laminate (0.69 versus 0.82 percent).

The 0/90 edge delamination growth was observed in each of the $(0_2/90_6)_s$ specimens tested and had a threshold strain range of 0.60 to 0.84 percent within the group. For the $(0_4/90_4)_s$ plies, the event was recorded in only one of the replicates.

The final matrix event to occur was the unstable propagation of the delamination in the length direction followed immediately by localized fiber breaks. Figures 4.13 and 4.14 display the edge views of the event, and figure 4.15 represents the event schematically. The event was bounded by the 0° ply split, 0/90 interface, and the free edge. Fiber breaks occurred close to the end tabs. Again, the $(0_2/90_6)_s$ experienced the event at a lower strain than did the $(0_4/90_4)_s$ (0.74 versus 1.0 percent). This was the last damage event observed before ultimate failure of the specimens.

The range of threshold strain for this event in the $(0_2/90_6)_s$ laminates was 0.61 to 0.87 percent. Again, the delamination/localized fiber break was only recorded for one of the three replicas in the $(0_4/90_4)_s$ specimens; the threshold strain was 1.0 percent.

Acoustic Emission Results

The following discussion is a typical representation of the results obtained for each of the two lay-ups. A description of the AE signature plots employed is presented. Figures 4.16 and 4.17 display the results of AE in the form of amplitude versus strain, energy versus strain, and cumulative counts versus strain. Note that the $(0_2/90_6)_s$ laminate plots contain gaps in the data because the load was held for a few seconds during x-ray exposure of the specimens tested early in the program. Also, the first laminate type was strained only to a point when all events of interest were observed and then the tests were ended. For the $(0_4/90_4)_s$ laminates, the tensile tests were continuous even during exposure and the laminates were studied up to failure.

For both cross-ply lay-ups, the AE signatures could not be used to discern the different matrix-dominated events, although fiber failures were recognized. In the plots of amplitude versus strain for the $(0_2/90_6)_s$ laminates, the majority of events occurred below 8000 dB and were indistinguishable. The peaks which occurred above 9600 dB were correlated with the edge view data and were recognized as fiber breaks. Signals were apparent at about 0.24 percent strain and steadily increased in amplitude and counts.

For the case of the $(0_4/90_4)_s$ laminates, the majority of events occurred below 6000 dB with distinct peaks for fiber breaks above 8000 dB (fig. 4.17(a)). Significant event occurrences for the lay-up began at about 0.75 percent strain and increased abruptly in amplitude level and cumulative counts.

In the plots of energy versus strain, the fiber breaks had midrange peaks as compared with the other events. The occurrences with the highest energy peaks could not be correlated with any observable cracking sequence in either lay-up. Because the energy of the AE signal is a function of time, a crack propagation such as delamination was the probable cause, although at this stage it could not be verified.

The plots of cumulative counts versus strain differed between the two lay-ups. The $(0_2/90_6)_s$ laminates showed a simple linear rise in cumulative counts whereas an exponential relationship was observed for the $(0_4/90_4)_s$ lay-up. For the exponential case, a slow accumulation of counts was observed until 0.80 percent, followed by a steep increase in activity up to failure.

31

(a)
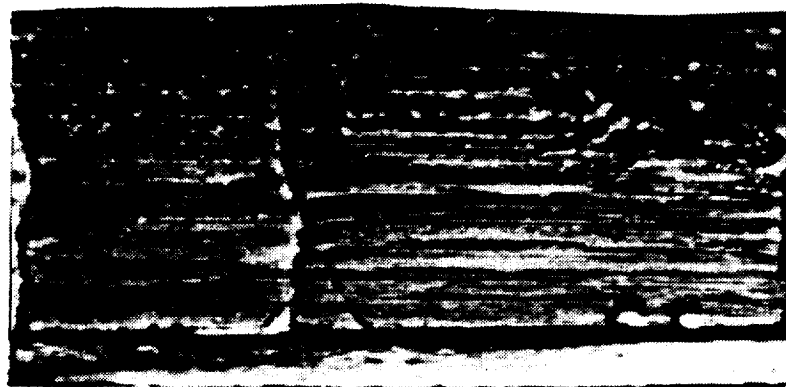
(b)

Figure 4.13.—Occurrence of edge delamination and localized fiber break in $(0_2/90_6)_s$ laminate. (a) Before. (b) After.

(a)

(b)

Figure 4.14.—Occurrence of edge delamination and localized fiber break in $(0_2/90_4)_s$ laminate. (a) Before. (b) After.
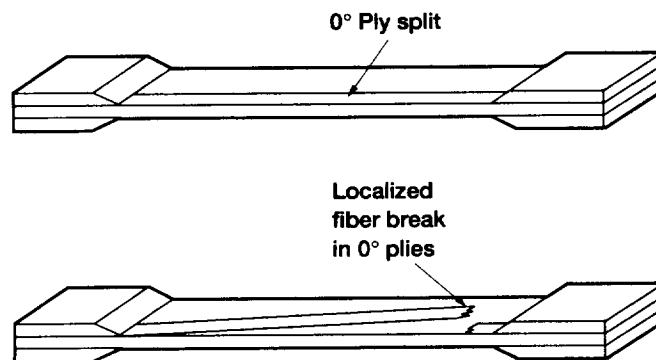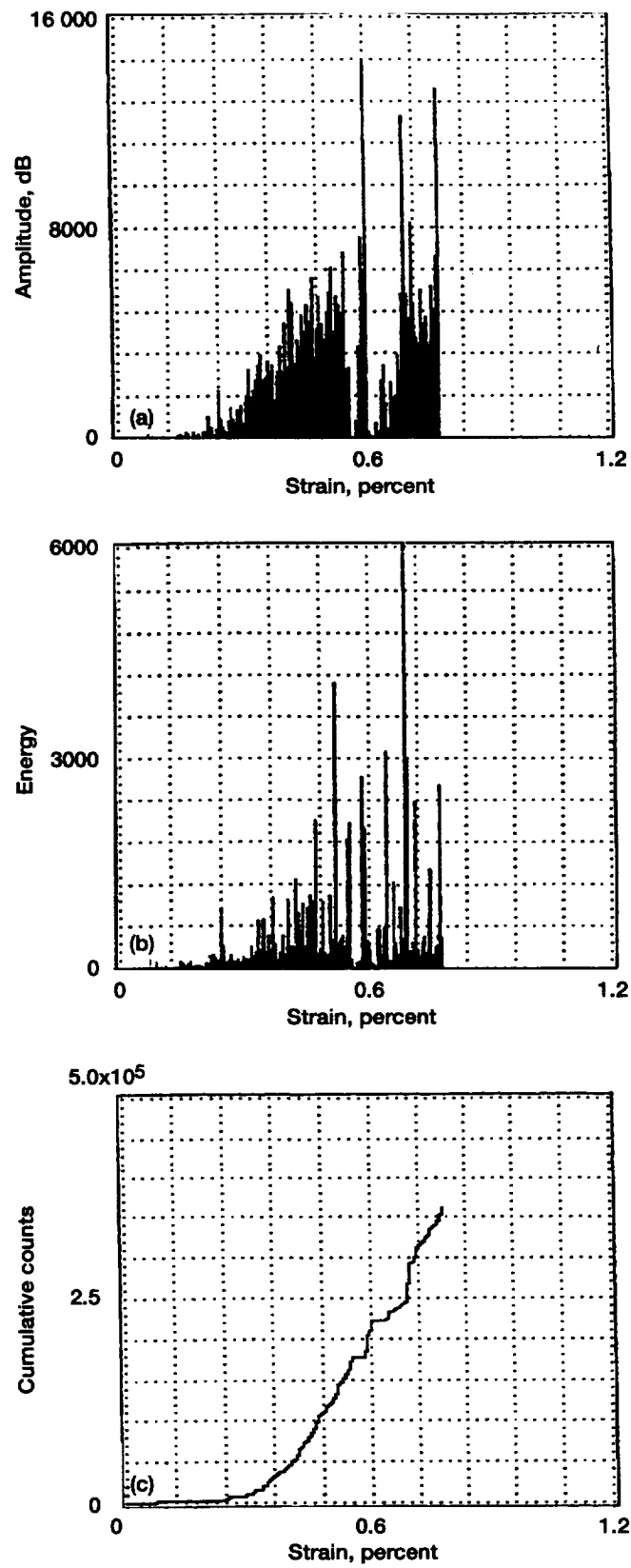

0° Ply split

Localized
fiber break
in 0° plies

Figure 4.15.—Localized fiber break.

Figure 4.16.—Acoustic emission data for $(0_2/90_6)_s$ laminate.
(a) Amplitude versus strain. (b) Energy versus strain.
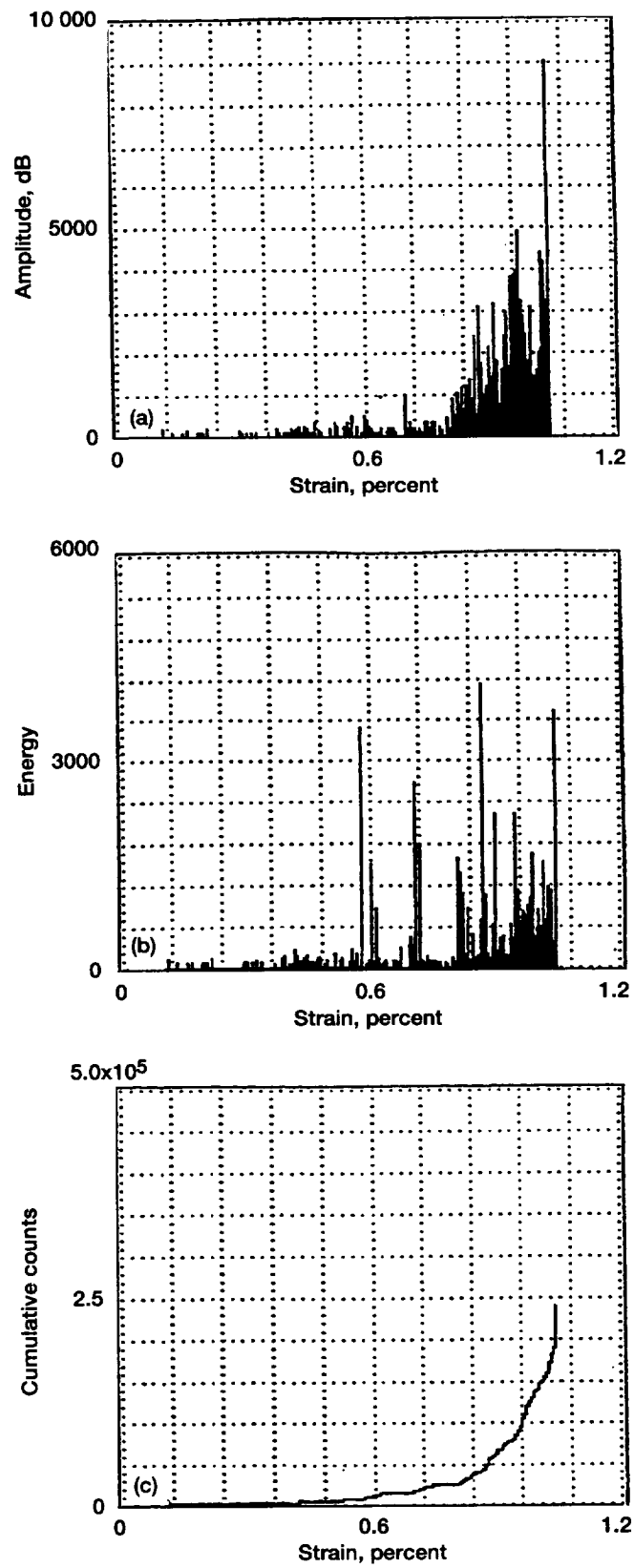(c) Cumulative counts versus strain.

Figure 4.17.—Acoustic emission data for $(0_4/90_4)_s$ laminate.
(a) Amplitude versus strain. (b) Energy versus strain.
(c) Cumulative counts versus strain.

For the analytical portion of this study, the finite element method of chapter III was employed to calculate the strain energy release rate (SERR) coefficient function for four matrix-dominated events. The events were secondary transverse cracks, longitudinal splitting, and two types of 0/90 delaminations: delaminations induced at the transverse crack and the free edge and those initiated at the crossing of a longitudinal split and transverse crack (see fig. 3.1). For each laminate, C_e and C_T curves were produced for the events of interest. The plots display the three individual components of the SERR coefficients (see eq. (3.8)) and the sum of these components which were utilized in equation (3.5).

The limitations of the NDE techniques prevented the observation of delaminations which developed within the specimen. Also, it was shown that transverse cracks and longitudinal splits were saturated before mechanical testing. Because of these drawbacks, the only event of interest experimentally observed was the 0/90 delaminations which initiated at the base of a transverse crack and the free edge. For this event, the test results were combined with the FE data to obtain the critical energy release rates for the crack.

Figures 4.18 to 4.25 present the finite-element-produced C_e and C_T curves for each case studied. Note that for simplicity, the $(0_1/90_3)_s$ and $(0_2/90_2)_s$ laminates were employed in the FE runs. To compensate for this, the linear scale factor t of equation (3.5) was replaced by $2t$.

The experimental results showed that transverse and longitudinal cracks were saturated before tensile testing; hence, no threshold strain data from the experiments was acquired. Because of this, only a description of the strain energy release rates for these events is given.

In the case of secondary transverse cracks, the C_e coefficients of both laminates revealed unstable growth. As an initial flaw propagates as the result of an applied uniaxial load, the available energy increases with crack size without any increase in the load. The flaw will instantaneously grow to the physical limits of size, which, for this case, was the free edge and the longitudinal plies.

The C_T function of the $(0_2/90_2)_s$ revealed unstable behavior for a flaw with a crack length of less than 1.6 (a/t). This was followed by stable propagation, meaning that the thermal load had to be increased to cause further growth. The $(0_1/90_3)_s$ displayed unstable crack growth throughout.

In the case of longitudinal splitting, the C_e for the $(0_1/90_3)_s$ was the only SERR curve with a stable growth. An initial flaw would propagate to a value of 1 (a/t) and then an additional load would be needed for further growth. At 2.0 (a/t), the C_e was again unstable. The C_T for the lay-up was unstable throughout. For the $(0_2/90_2)_s$ laminate, both the C_e and the C_T curves were unstable.

In both transverse and split cracks, the SERR due to thermal loading was the dominating term. This was obvious from the fact that both events were saturated with cracks before mechanical loading. Also, because each SERR was dependent only on the component of the load which was transverse to the crack propagation, the fracture events were primarily mode I. Hence, it was assumed that these two events had equivalent G_C values.
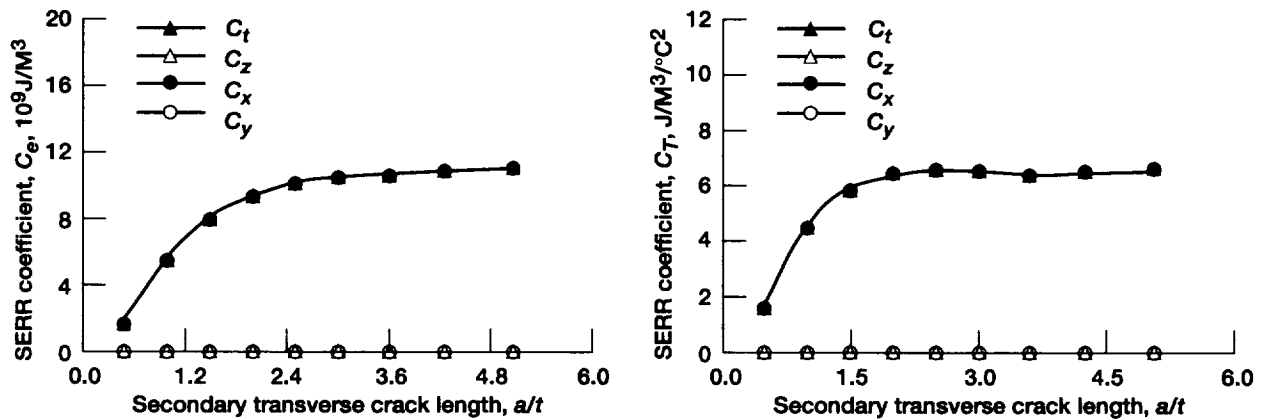

Figure 4.18.—Strain energy release rate (SERR) coefficients C_e and C_T for secondary transverse cracking in $(0_1/90_3)_s$ laminate.
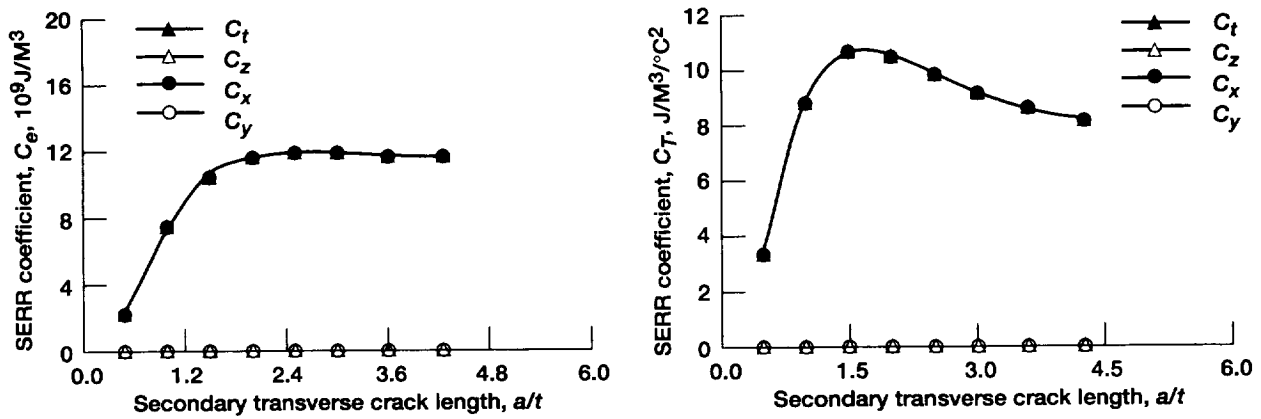
Figure 4.19.—Strain energy release rate (SERR) coefficients C_e and C_T for secondary transverse cracking in $(0_2/90_2)_s$ laminate.
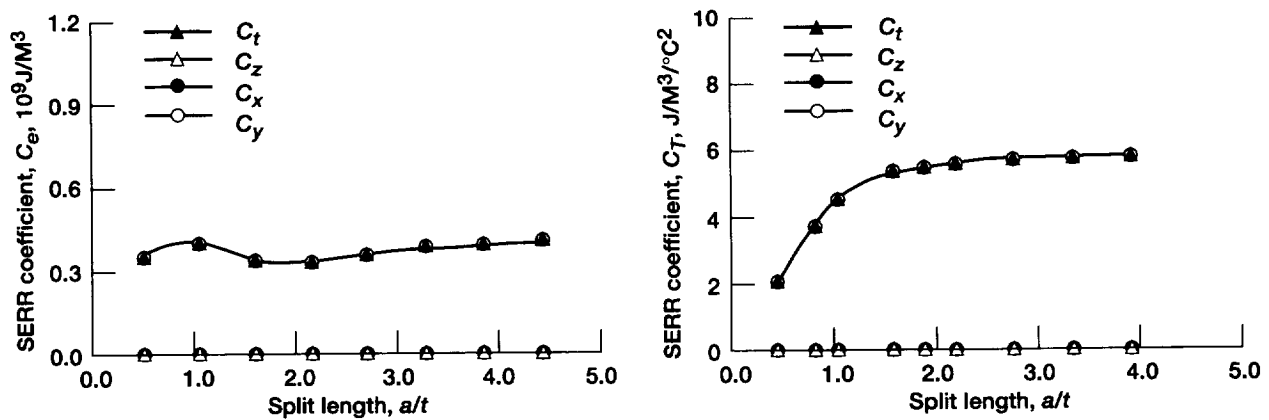

Figure 4.20.—Strain energy release rate (SERR) coefficients C_e and C_T for longitudinal split in $(0_1/90_3)_s$ laminate.
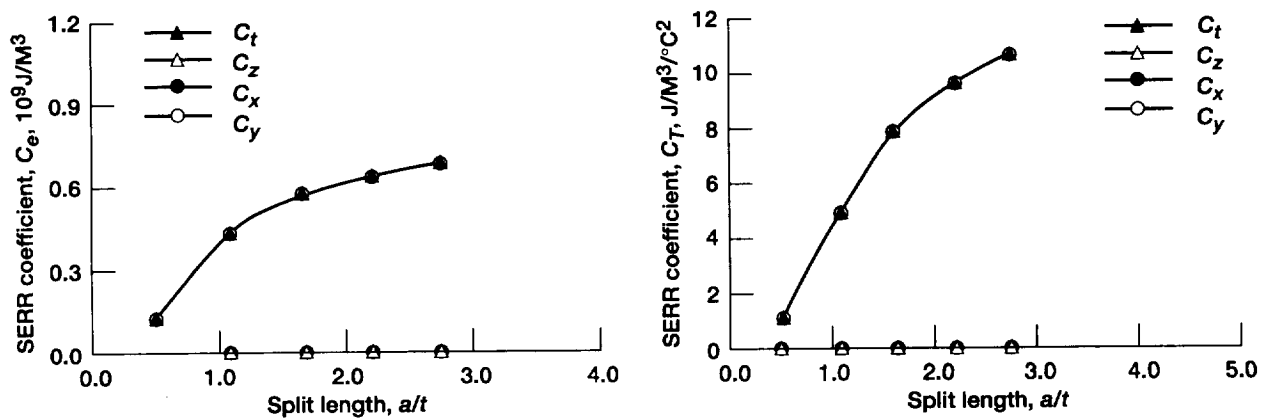

Figure 4.21.—Strain energy release rate (SERR) coefficients C_e and C_T for longitudinal split in $(0_2/90_2)_s$ laminate.
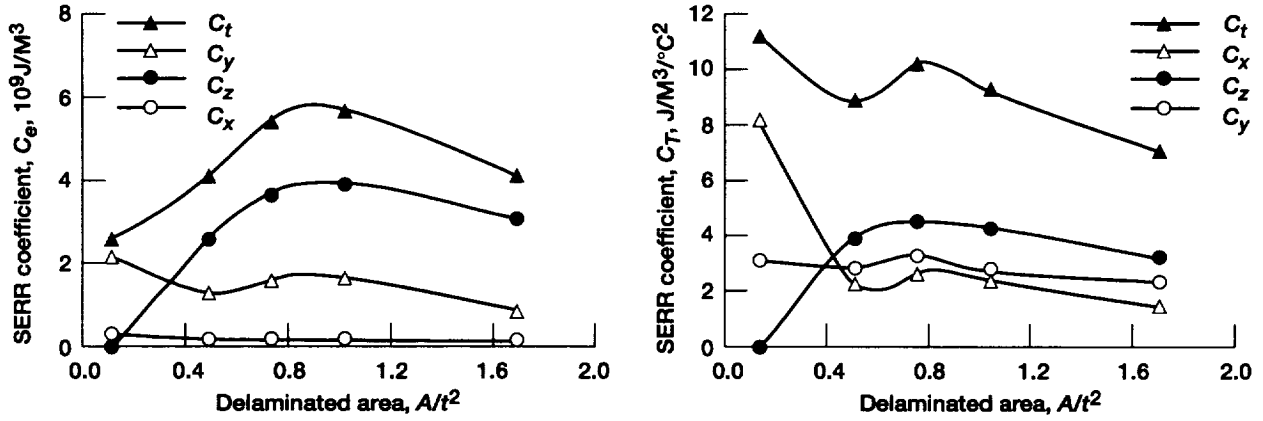
Figure 4.22.—Strain energy release rate (SERR) coefficients C_e and C_T for 0/90 delamination at transverse crack and split crossing point in $(0_1/90_3)_s$ laminate.
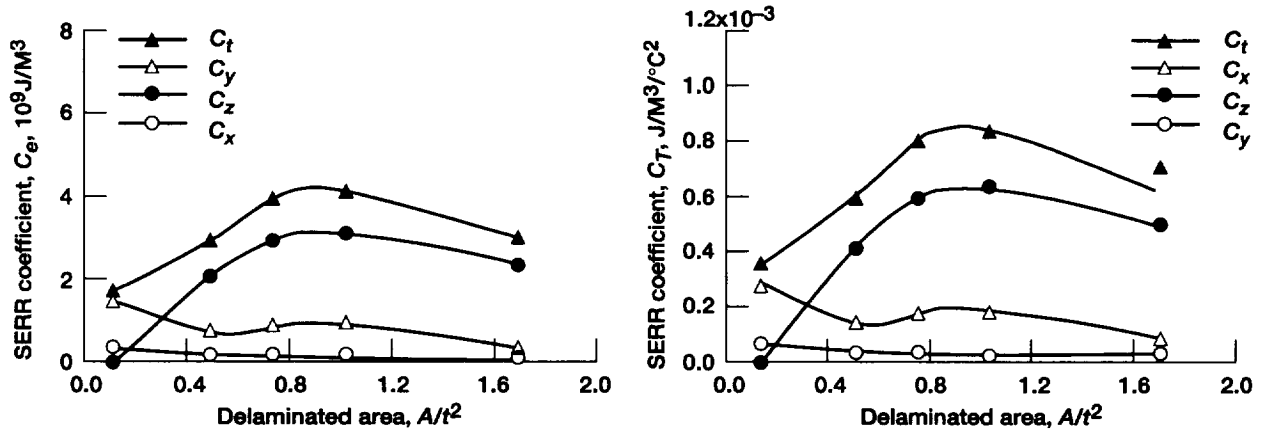

Figure 4.23.—Strain energy release rate (SERR) coefficients C_e and C_T for 0/90 delamination at transverse crack and split crossing point in $(0_2/90_2)_s$ laminate.
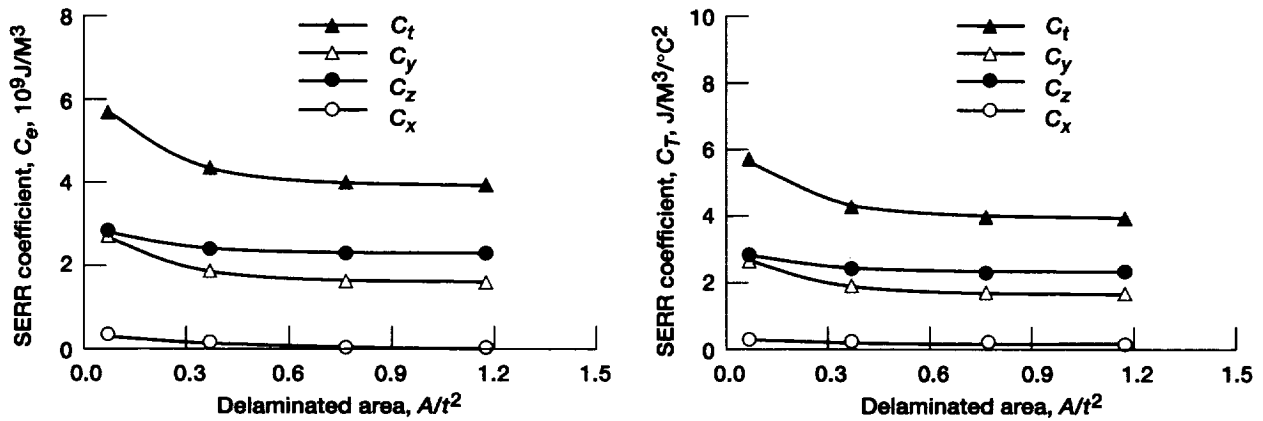

Figure 4.24.—Strain energy release rate (SERR) coefficients C_e and C_T for free-edge 0/90 delamination in $(0_1/90_3)_s$ laminate.
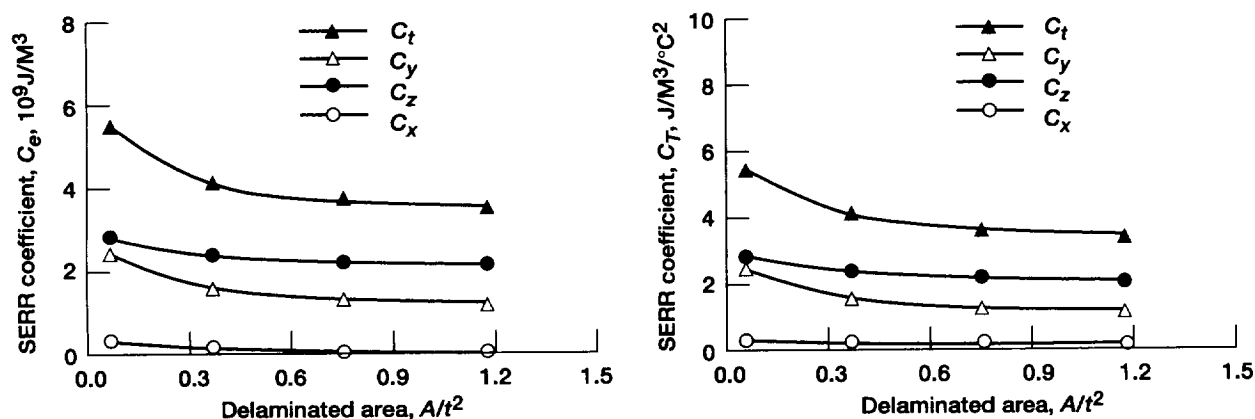
38

Figure 4.25.—Strain energy release rate (SERR) coefficients C_e and C_T for free-edge 0/90 delamination in $(0_2/90_2)_s$ laminate.

For the split-induced delamination, the C_e curves for both lay-ups showed unstable crack propagation up to a size of 0.9 $(A/t^2$ where A is area) followed by stable growth, but the C_T curves differed. Values for thermal SERR in the $(0_2/90_2)_s$ ply were near zero and were minor when compared to the SERR due to mechanical load. However, for the $(0_1/90_3)$ laminate, the thermal loads were still large with respect to mechanical loads.

Free-edge 0/90 delamination was the only event which could be analyzed both analytically and experimentally. For both laminate types, the C_e and C_T curves showed stable growth. The experimental observations also showed stable growth except for near failure loads. At this point, propagation was unstable and was probably the result of the interaction of multiple events which occurred near the ultimate laminate stress.

Wang, Chou, and Lei (1984) stated that a delamination is observable when the crack area is about 1 (A/t^2). Hence, from figures 4.24 and 4.25, the following values were obtained:

For the $(0_1/90_3)_s$ laminate,

$$C_e \text{ at } 1.0 \ (A/t^2) = 4.0\times10^9 \text{ J m}^{-3}$$
$$C_T \text{ at } 1.0 \ (A/t^2) = 4.0 \text{ J m}^{-3} \ ^\circ\text{C}^{-2}$$

For the $(0_2/90_2)_s$ laminate,

$$C_e \text{ at } 1.0 \ (A/t^2) = 3.5\times10^9 \text{ J m}^{-3}$$
$$C_T \text{ at } 1.0 \ (A/t^2) = 3.8 \text{ J m}^{-3} \ ^\circ\text{C}^{-2}$$

Using values from table V for threshold strains, $\Delta T = 325 \ ^\circ\text{C}$, and $2t = 2.82\times10^{-4}$ and solving equation (3.5) gave the following values:

For the $(0_2/90_6)_s$ laminate,
$$G_C = 333 \text{ J m}^{-3}$$

For the $(0_4/90_4)_s$ laminate,
$$G_C = 354 \text{ J m}^{-3}$$

From these results it was seen that equation (3.5) was consistent and correlated well for both specimen types. Because both lay-ups had similar shaped coefficient functions and mode ratios, the critical energy release rates were expected to be about equal. The slight discrepancy was probably the result of the quality and statistical aspect of the manufacturing process.

39

CHAPTER V

SUMMARY AND FUTURE DIRECTION

Cross-ply pretest damage due to high-temperature processing was observed in the form of transverse and longitudinal cracks. Also, shear-induced angled cracks existed in the 90° plies and were located at the base of the transverse cracks. After loading the laminates, it was concluded that the transverse and longitudinal damage was saturated before any mechanical loads were applied. The only fracture events which propagated further were delaminations and the unexpected angled cracks. Observation of the damage was carried out using the nondestructive evaluation (NDE) techniques of acoustic emission, in situ x radiography, and real-time edge view microscopy.

The signatures of the acoustic signal utilized were amplitude and energy, neither of which made it possible to discern between the matrix-dominated events of interest although fiber breaks did show up as distinct high peaks in the amplitude-versus-strain plots. The discontinuities due to the existing damage were assumed to cause attenuation effects in the AE signatures; hence, the difficulties in matrix event identification.

In situ x radiography was able to identify transverse and longitudinal cracks clearly whereas delaminations and angled cracks were not recognized. Hence, delaminations occurring at the transverse crack and split crossing points were not detected during the testing. The density of the fluorescent dye and its capability in penetrating narrow crack spacing was the probable cause of the detection difficulties. For future experiments, higher density dyes should be employed when events with limited crack openings are examined.

Real-time edge view microscopy proved the most reliable source of information in this study. Further propagation of angled cracks and free-edge 0/90 delaminations were observed and recorded on video tape at a magnification of 50. The threshold strains at the occurrence of these events were also obtained. Because the method could not be used to inspect the depth of the cracks into the specimen, the total surface areas of the events were not known. The technique provided positive results although a second NDE method was needed to yield the information concerning the area.

The experimental data obtained on the onset of damage in the cross-plies showed the events to be dependent on the 90° plies thickness. All matrix damage events occurred at lower threshold strains in the cross-ply containing the thicker 90° layers. As observed by the edge view method, the angled cracks transpired first, followed by the onset of free-edge 0/90 delamination. After a period of stable propagation, unstable growth ensued and emulated into localized fiber failures. These fiber breaks were the last event before ultimate laminate failure.

The analytical model simulated the systems of interest including the initial transverse cracks, and it was used to obtain the nondimensional strain energy release rate coefficients (SERR). By inducing the finite element model to unite thermal and mechanical loads, the SERR coefficient curves were produced.

Because of the limitations in the NDE techniques and the pretest saturation of transverse and longitudinal cracks, only the cases of free-edge 0/90 delamination were compared with the experimental results. The threshold strains obtained from the experiments and the SERR coefficient curves were used to calculate the critical strain energy release rates for the case of free-edge 0/90 delamination in the two different cross-plies. Although the threshold strains and the SERR curves were different for the two lay-ups, their critical strain energy release rates were essentially equal because their SERR curves had similar shapes and mode ratios (G_I/G_{II}, G_I/G_{III}).

Future directions involve further study of the SERR curves for different events, loading conditions, and laminate lay-ups. By such investigations, analytical relationships can be developed between the critical strain energy release rates and the characteristics of the SERR curves for a given material.

A thorough experimental and analytical examination of the angled cracks needs to be completed. Such a study will enable a better understanding of the event and its interaction with other matrix-dominated fractures. Also required are NDE methods which can reliably measure the area of a crack such as delamination. Further refinement of the techniques employed for this study or the introduction of new NDE techniques is needed.

REFERENCES

Agarwal, Bhagwan, D.; and Broutman, Lawrence, J.: Analysis and Performance of Fiber Composites. Second ed. John Wiley & Sons, Inc., 1990.

Aveston, J.; and Kelly, A.: Theory of Multiple Fracture of Fibrous Composites. J. Materials Sci., vol. 8, 1973, pp. 352–362.

Awerbuch, J.; Perkinson, H.E.; and Kamel, I.H.: Deformation Characteristics and Failure Modes of Notched Graphite Polyimide Composites at Room and Elevated Temperatures. (Drexel University; NASA Grant NSG–1606.) NASA CR–159375, Aug. 1980.

Baaklini, G.Y.: X-Ray Attenuation Measurements for High Temperature Materials Characterization and In-Situ Monitoring of Damage Accumulation. NASA TM–105577, March 1992.

Bader, M.G., et al.: The Mechanisms of Initiation and Development of Damage in Multiaxial Fibre-Reinforced Plastics Laminates. Proceedings of the Third International Conference on Mechanical Behaviour of Materials, Oxford, vol. 3, 1979, pp. 227–239.

Bailey, J.E.; Curtis, P.T.; and Parvizi, A.: On the Transverse Cracking and Longitudinal Splitting Behaviour of Glass and Carbon Fibre Reinforced Epoxy Crossply Laminates and the Effect of Poisson and Thermally Generated Strain. Proceedings of the Royal Society, London, vol. 366, no. 1727, 1979, pp. 599-623.

Block, J.: Characterization of Damage Progression in Fibre Reinforced Composites by Acoustic Emission. Engineering Applications of New Composites, Omega Scientific, Wallingford, England, 1988, pp. 340–346.

Broek, D.: Elementary Engineering Fracture Mechanics. Martinus Nijhoff, Hingham, Massachusetts, 1986.

Carlsson, L.A.; and Pipes, R.B.: Experimental Characterization of Advanced Composite Materials. Prentice-Hall, Englewood Cliffs, New Jersey, 1987.

Crossman, F.W., et al.: Initiation and Growth of Transverse Cracks and Edge Delamination in Composite Laminates, Part II—Experimental Correlation. J. Compos. Mater. Suppl., vol. 14, no. 1, 1980, pp. 88–108.

Crossman, F.W.; Warren, W.J.; and Wang, A.S.D.: Influence of Ply Thickness on Damage Accumulation and Final Fracture. 1983 Advances in Aerospace Structures, Materials and Dynamics: A Symposium on Composites, ASME AD–06, 1983, pp. 215–226.

Duesing, L.A.: Acoustic Emission Testing of Composite Materials. Proceedings of the Annual Reliability and Maintainability Symposium, IEEE, 1989, pp.128–134.

Flaggs, D.L.; and Kural, M.H.: Experimental Determination of the In-Situ Transverse Lamina Strength in Graphite/Epoxy Laminates. J. Compo. Mater., vol. 16, March 1982, pp. 103–116.

Harrison, R.P.; and Bader, M.G.: Damage Development in CFRP Laminates Under Monotonic and Cyclic Stressing. Fibre Sci. Technol., vol. 18, 1983, pp. 163–180.

Irwin, G.R.: Fracture. Handbuch der Physik. S. Flügge, ed., vol. VI, Springer-Verlag, 1958, pp. 551–590.

Jeng, J.S.; Kanji, O.; and Yang, J.M.: Fracture Mechanism Studies of Carbon/PMR-15 Composites by Acoustic Emission. J. Acoust. Emiss., vol. 8, 1989, pp. 268–271.

Papadopoulos, D.S.; and Bowles, K.J.: Use of Unbalanced Laminates as a Screening Method for Microcracking. NASA TM–102517, 1990.

Rajan, D.S.; Kishore, N.N.; and Agarwal, B.D.: Damage Characterization in Kevlar/Epoxy Composites Using Acoustic Emission Technique. J. Acoust. Emiss., vol. 8, 1989, pp. 297–300.

Reifsnider, K.L., et al.: Fatigue Damage-Strength Relationships in Composite Laminates. AFWAL TR–83–3084, Air Force Wright Aeronautical Laboratories, Ohio, 1983.

Rybicki, E.F.; and Kanninen, M.F.: A Finite Element Calculation of Stress Intensity Factors by a Modified Crack Closure Integral. Eng. Fract. Mech., vol. 9, no. 4, 1977, pp. 931–938.

Rybicki, E.F.; Schmueser, D.W.; and Fox, J.: An Energy Release Rate Approach for Stable Crack Growth in the Free-Edge Delamination Problem. J. Compos. Mater., vol. 11, Oct. 1977, pp. 470-487.

Simpson, M.; Jacobs, P.M.; and Jones, F.R.: Generation of Thermal Strains in Carbon Fiber-Reinforced Bismaleimide (PMR-15) Composites, Part I—The Determination of Residual Thermal Strains in Cross-Ply Laminates. Composites, vol. 22, March 1991, pp. 89-97.

Wang, A.S.D.; Chou, P.C.; and Lei, S.C.: A Stochastic Model for the Growth of Matrix Cracks in Composite Laminates. J. Compos. Mater., vol. 18, May 1984, pp. 239–254.

Wang, A.S.D.; and Crossman, F.W.: Fracture Mechanics of Sublaminate Cracks. AFOSR–83–0594TR, 1982.

Wang, A.S.D.; and Crossman, F.W.: Initiation and Growth of Transverse Cracks and Edge Delamination in Composite Laminates, Part I—An Energy Method. J. Compos. Mater. Suppl., vol. 14, no. 1, 1980, pp. 71–87.

Wang, A.S.D.; Kishore, N.N.; and Li, C.A.: Crack Development in Graphite-Epoxy Cross-Ply Laminates Under
Uniaxial Tension. Comp. Sci. T., vol. 24, no. 1, 1985, pp. 1–31.

Wang, A.S.D.; Slomiana, M.; and Bucinell, R.: A Three-Dimensional Finite Element Analysis of Delamination
Growth in Composite Laminates, Part 1: The Energy Methods and Case-Study Problems. NADC-84017-60,
Naval Air Development Center, Pennsylvania, 1983.

REPORT DOCUMENTATION PAGE

Public reporting burden for this collection of information is estimated to average 1 hour per response, including the time for reviewing instructions, searching existing data sources, gathering and maintaining the data needed, and completing and reviewing the collection of information. Send comments regarding this burden estimate or any other aspect of this collection of information, including suggestions for reducing this burden, to Washington Headquarters Services, Directorate for Information Operations and Reports, 1215 Jefferson Davis Highway, Suite 1204, Arlington, VA 22202-4302, and to the Office of Management and Budget, Paperwork Reduction Project (0704-0188), Washington, DC 20503.

1. AGENCY USE ONLY (Leave blank)	2. REPORT DATE January 1996	3. REPORT TYPE AND DATES COVERED Final Contractor Report

4. TITLE AND SUBTITLE

Crack Development in Cross-Ply Laminates Under Uniaxial Tension

5. FUNDING NUMBERS

WU–505–62–2B
G–NAG3–1543

6. AUTHOR(S)

Andrew L. Gyekenyesi

7. PERFORMING ORGANIZATION NAME(S) AND ADDRESS(ES)

Cleveland State University
Cleveland, Ohio 44115

8. PERFORMING ORGANIZATION REPORT NUMBER

E–9635

9. SPONSORING/MONITORING AGENCY NAME(S) AND ADDRESS(ES)

National Aeronautics and Space Administration
Lewis Research Center
Cleveland, Ohio 44135–3191

10. SPONSORING/MONITORING AGENCY REPORT NUMBER

NASA CR–195464

11. SUPPLEMENTARY NOTES

This report was submitted as a thesis in partial fulfillment of the requirements for the degree Master's of Science in Engineering Mechanics to Cleveland State University, Cleveland, Ohio. Project Manager, J. R. Ellis, Structures Division, NASA Lewis Research Center, organization code 5220, (216) 433–3340.

12a. DISTRIBUTION/AVAILABILITY STATEMENT

Unclassified - Unlimited
Subject Category 39

This publication is available from the NASA Center for Aerospace Information, (301) 621–0390.

12b. DISTRIBUTION CODE

13. ABSTRACT (Maximum 200 words)

This study addresses matrix-dominated failures in carbon fiber/polymer matrix composite laminates in a cross-ply lay-up. The events of interest are interlaminar fracture in the form of transverse cracks in the 90° plies and longitudinal splitting in the 0° plies and interlaminar fracture in the form of 0/90 delamination. These events were observed using various nondestructive evaluation (NDE) techniques during static tensile tests. Acoustic emission (AE) x radiography, and edge view microscopy were the principal ones utilized in a real-time environment. A comparison of the NDE results with an analytical model based on the classical linear fracture mechanics concept of strain energy release rate as a criterion for crack growth was performed. The virtual crack closure theory was incorporated with a finite element model to generate strain energy release rate curves for the analytical case. Celion carbon fiber/polyimide matrix (G30-500/PMR-15) was the material tested with cross-ply lay-ups of $(0_2/90_6)_s$ and $(0_4/90_4)_s$. The test specimens contained thermally induced cracks caused by the high-temperature processing. The analytical model was updated to compensate for the initial damage and to study further accumulation by taking into account the crack interactions. By correlating the experimental and analytical data, the critical energy release rates were found for the observable events of interest.

14. SUBJECT TERMS

Static tensile tests; Cross-ply laminates; Delamination; Strain energy release rate; Finite element modeling; NDE; X radiography; Acoustic emission; Edge view microscopy

15. NUMBER OF PAGES
44

16. PRICE CODE
A03

17. SECURITY CLASSIFICATION OF REPORT Unclassified	18. SECURITY CLASSIFICATION OF THIS PAGE Unclassified	19. SECURITY CLASSIFICATION OF ABSTRACT Unclassified	20. LIMITATION OF ABSTRACT

NSN 7540-01-280-5500

Standard Form 298 (Rev. 2-89)
Prescribed by ANSI Std. Z39-18
298-102

National Aeronautics and
Space Administration

Lewis Research Center

21000 Brookpark Rd.
Cleveland, OH 44135-3191